Research on the Stability, Electronic Properties, and Structure of a-Si:H and Its Alloys

Annual Subcontract Report
1 June 1992 – 31 May 1993

W. B. Jackson, N. Johnson, N. Nickel,
C. Nebel, M. Hack, P. Santos,
G. Schumm, R. A. Street, R. Thompson,
C. C. Tsai, J. Walker
Xerox Palo Alto Research Center
Palo Alto, California

MASTER

This publication was reproduced from the best available camera-ready copy
submitted by the subcontractor and received no editorial review at NREL.

NOTICE

Printed in the United States of America
Available from:
National Technical Information Service
U.S. Department of Commerce
5285 Port Royal Road
Springfield, VA 22161

Price: Microfiche A01
Printed Copy A04

Codes are used for pricing all publications. The code is determined by the number of pages in the publication. Information pertaining to the pricing codes can be found in the current issue of the following publications which are generally available in most libraries: *Energy Research Abstracts (ERA); Government Reports Announcements and Index (GRA and I); Scientific and Technical Abstract Reports (STAR)*; and publication NTIS-PR-360 available from NTIS at the above address.

Printed on recycled paper

DISCLAIMER

Portions of this document may be illegible electronic image products. Images are produced from the best available original document.

TABLE OF CONTENTS

page.

EXECUTIVE SUMMARY

Our research during this period focusses on defect and transport properties of a-Si:H with particular emphasis on defect metastability. Light-induced defects remain the major impediment to higher stabilized solar cell efficiencies. The many years of research have shown that this is a difficult problem to solve and we take the view that a solution can be found only with a deep understanding of the mechanism, and this has been our main goal. The metastability is closely related to the intrinsic defect properties and so these studies have also led to a greatly improved model of all the electronic properties of a-Si:H.

In section A of the report we give further theoretical analysis of the defect pool model for the equilibrium dark defect density, with particular reference to whether there are significant charged defects. The defect pool analysis tends to favor charged defects, but with a density that depends on the energy distribution of defects and on their correlation energy. We have made ESR studies to count the different charge states and conclude that there may be as many as 5 times more charged than neutral defects.

We have studies how the defects and metastability depend on the material stucture, specifically by comparing as-depositied and post-deuterated films. Interestingly there are no observable differences despite the introduction of a large quantity of hydrogen, which shows that hydrogen is incorporated into the structure without perturbing the weak bond distribution.

The techniques we developed earlier to measure defects from the reverse bias thermal generation current are valuable because metastability is studied in a solar cell configuration. Comparison of light-induced and current-induced metastability confirms that the same defects are created, consistent with their being induced by the same recombination process. However, the reverse bias current-voltage characteristics indicate that the spatial distribution of the defects is different, with light-induced defects tending to be formed close to the illuminated contact. This has the effect of increasing the reverse current because of contact injection effects. Current induced defects are evidently distributed more uniformly.

Numerical simulations play an increasingly important role in a-Si:H research. Simple analytical models are typically not accurate enough for data analysis because of the distribution of states. As desribed in section B, we routinely use an electronic transport model to analyse forward and reverse currents and have extended this to the calculation of field dependences of bulk and contact currents, which give more precision to our analysis of defect from reverse bias thermal generation currents. We have now developed a numerical model for hydrogen transport and have applied this to H diffusion to derive information about the hydrogen density of states.

Electronic transport is discussed in section C. The Hall effect remains the least understood physical phenomenon in a-Si:H due to its anomalous sign. We have measured the Hall effect in a-Si:H and a-Si:C:H alloys. Despite the anomaly, we infer from various tests that the Hall mobility is a true reflection of the free carrier mobility. We show that the mobility decreases as the band tails broaden, and suggest that the the mobility is proportional to the slope ($\mu_H \sim 1/E_o$), because the slope is a measure of the disorder. Confirmation of this interpretation would allow the Hall effect to become a very useful characterization tool.

We have completed a lengthy study of transport at low temperatures and high electric fields with a study of space charge limited currents. There is now a rather complete understanding of the field dependent transport in the hopping regime. To date no solar cells models include field dependent transport, and it remains to be seen whether this is important limitations to the models.

Experimental evidence continues to make it very clear that hydrogen mediates the defect metastability. We therefore continue to explore H transport and bonding and this work is described in section D. The basic hydrogen diffusion properties are now well known and we are focussing on the details of the trasport through studies of the effects of injecting or depleting hydrogen in the material. The results show that H binds to deep traps but that the traps are probably not simple dangling bonds. Indeed, the addition of H clearly forms new traps, so that there is a structural change that allows the extra hydrogen to be accomodated without change in the disorder, possibly by increasing the size of voids.

Light-induced H diffusion is perhaps the most direct link between metastability and hydrogen motion. This shows that there is a strong interaction between

hydrogen and the electronic carriers - an electron-structure interaction which underlies the metastable changes. We have continued this work by measuring the suppression of hydrogen diffusion under reverse bias, which provides a further demonstration that electron-hole pair recombination is needed for H diffusion. The results show that the trapping of mobile H is suppressed by the reverse bias and that the mean free path is about 400Å. This result may have some implications for defect creation in solar cells whose thickness is not very much larger than the hydrogen diffusion length.

Finally we have made first principles LDA calculations of Si-H binding energies to validate the hydrogen density of sates model and to analyse H diffusion. At present, however, the experimental and theoretical energies are not fully reconciled, and this remains a challenge to our understanding of hydrogen in a-Si:H.

LIST OF FIGURES

barrier energies while the dashed line represents the behavior for a distribution of sites communicating with a single extended transport level. The dot-dashed line indicates the initial slope of the decay for this model.

Fig. 9   The total change in carrier concentration divided by the equilibrium carrier concentration for the indicated measurement temperatures. The line represents the results of a simulation with a distribution of barriers and sites.

Fig. 10   CPM data showing the increase of the sub-gap absorption after current-induced defect formation. The Urbach edge region is unchanged.

Fig. 11   Reverse bias current-voltage (J-V) characteristics of a p-i-n diode after various stages of light and current induced defect generation, as indicated.

Fig. 12   Plot of the relative defect densities obtained from CPM and reverse current measurements showing linear behavious but with an offset between the two types of defect creation.

Fig. 13   Numerical calculation of the J-V characteristics assuming a Poole-Frenkel enhancement of the thermal generation current, and no contact injection. The assumed degradation factors of the three regions of the sample are shown.

Fig. 14   Numerical calculation of the J-V characteristics assuming a tunneling enhancement of the injection current. The assumed degradation factors of the three regions of the sample are shown.

Fig. 15   Hall mobility, H, conductivity, σ, and Hall carrier density, n_H, measured as a function of temperature.

Fig. 16   Variations of μ_D, μ_H, N_{BT}, σ and n_H as a function of annealing temperature.

Fig. 17   Hall mobility in a-Si:C.

Fig. 18   Space charge limited currents measured at T = 10 K and 80 K on n+-i-n+ (electrons) and p+-i-p+ (holes) junction.

Fig. 19   Electron transient space charge limited currents measured at T= 80 K on the 2.5 µm (a) and 3.5 µm (b) thick n+-i-n+ junctions. Arrows indicate the transit time.

Fig. 20   Electron drift mobilities deduced at t = 80 K by transient space charge limited currents on n+-i-n+-junctions of thickness 2.5 and 3.5 µm and by time-of-flight experiments on p-i-n junctions of 2 and 10 µm thickness.

Fig. 21   (a) and (b) The deuterium concentration versus distance for exposure to a deuterium plasma and a plasma attenuated by a stainless steel mesh at indicated temperatures and times. (a) H-depleted a-Si:H. (b) as-deposited a-Si:H subjected to plasma at a temperature of 275C, for 3 hrs. The top solid line indicates an erfc profile. (c) Deuterium profiles after exposure to an attenuated deu-terium plasma for both a-Si:H and H-depleted a-Si. The sub-strate temperature for dep-osition of the a-Si:H was 380C.

Fig. 22   Effect of time on D diffusion profiles. D concentration versus distance for various time for H-depleted a-Si. The H concentration for the first curve is also indicated. The solid line represents the best fit erfc to the data. The concentration where the data deviates from an erfc profile indicates the trap density which does not appear to change with time.

Fig. 23   Comparison of lay-er diffusion and diffusion from a plasma for a-Si:H.

Fig. 24   Effect of H concentration on the diffusion of D in H-depleted a-Si. The H was introduced by 2.5 hrs, 430 C remote plasma exposure at various attenuations. The H concentration profiles are also shown along with the estimated trap concentrations and a least squares erfc.

Fig. 25   Effect of extended annealing on the D diffusion profiles for two different samples a-Si:H samples with slightly different H con-centrations. The annealing times at 350C in hours preceding deuteration are indicated.

Fig. 26   Comparison of D diffusion in H-depleted Si, polycryst-alline Si, and c-Si containing H platelet nucleation sites. The c-Si sample was n-type Si, (100), float zone with a [P] =8X1017 cm-3 exposed to a D plasma at 150C, 20 min then at 275C, 60 min. The poly cryst-alline Si sample con-sisted of fine grained poly-Si un-doped and deuterated at 250C 30 min/, The H-depleted

a-Si was deuterated in an attenuated deu-terium plasma at 320 C for 30min.

Fig. 27 First-principles energies for various configurations of H in silicon. The zero of energy corresponds to a free H atom.

Fig. 28 A hydrogen trap model accounting for experimental results. The transport sites at the transport energy have an energy Em, while the shallow traps which release in a time short compared to the experiments are at energy Es. The deep states (energy Et) are in general separated from the shallow states. In H-depleted a-Si, the dangling bond states are significantly deeper than the shallower states occurring in normal a-Si:H which scale with H concentration. The hydrogen chemical potential, μ_H separates the occupied sites from the unoccupied sites from the unoccupied ones and resides in an approximate minimum of the density of trapping sites.

Fig. 29 The effect of decreasing the trap energy until it merges with the shallow traps.

Fig. 30 (a) Deuterium profiles for difusion in the intrinsic layer of a p-i-n diode under open circuit (oc) and reverse bias. (b) corresponding profiles under illumination.

Fig. 31 Effective and fictive diffusion coefficients for hydrogen diffusion under open circuit and under different bias and illumination conditions.

Fig. 32 Deuterium concentration profile in the tail region for different applied bias. The dashed and solid lines are the corresponding profiles in an unannealed control, sample and in a sample annealed under open-circuit conditions.

Fig. 33 Deuterium concentration profiles in p-i-n diodes annealed under fixed reverse bias of 5V at different temperatures. The solid line is a profile for an as-grown sample. The samples have deuterated n and p contacts.

Fig. 34 Time dependence of the deuterium profiles after annealing ata fixed reverse bias of 5V.

Stability, Electronic Properties and Structure of a-Si:H and its Alloys

A. DEFECT METASTABILITY AND EQUILIBRIUM

Continuing studies of defect and dopant metastability at Xerox PARC are described in this section. The properties of hydrogen and its relation to metastability are described in section D, and simulations of hydrogen transport are described in section B.

1. The Defect Pool Model and Charged Defects in Amorphous Silicon

Although the microscopic details of the defect creation processes are still debated, it is now well established that the defect structure in a-Si:H can be described by a chemical equilibrium reaction between defects (dangling Si bonds) and defect-free coordinations (Si-Si, Si-H bonds). Chemical equilibration in combination with a statistical distribution of sites where defects can be created, the so called defect pool, leads to a defect density-of-states $D(E)$ that generally is different from the pool distribution $P(E)$. We have compared the predictions of the defect pool model with ESR measurements to identify the role of charged defects in a-Si:H.

A number of reactions based on a specific structural reconfiguration but creating defects of different charge states may take place. For example, assume that some precursors, say weak-bonds, break into db's.

$$(e+h)+wb \rightleftharpoons D^0, \ e+wb \rightleftharpoons D^-, \ h+wb \rightleftharpoons D^+$$
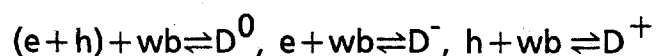
(In fact, each wb breaks into 2 dbs, and Si-H bonds may be involved, which leads to certain modifications of the results discussed below.) In doped material, where the majority of defects occurs in a single charge state, considering only the reaction that produces defects in that specific charge state and neglecting the others yields a sufficiently accurate description of the defect structure. In undoped a-Si, however, all of the above reactions may occur simultaneously. More important, substantial electronic reoccupation of defects created in a specific charge state may take place

1

during structural equilibration, depending on the energy position of the defect state with respect to the Fermi level. A general solution of equilibrium is obtained by appropriate coupling of the above reactions using Fermi occupation statistics. The law of mass action for the first reaction, gives

$$\frac{[D^0]}{[e][h][wb]} = \frac{f^0 N_D}{n\,p\,(N_t - N_D)} = exp\left(-\frac{\Delta G}{kT}\right) \qquad (1)$$

where $\Delta G = \Delta H - T\Delta S$ is the free energy of formation, N_t is the density of precursors before any are converted to defects, N_D is the total, $f_0 N_D$ is the neutral defect density determined by the probability for single occupation f_0, and np is the density of free carriers. All the other possible reactions are automatically taken care of by subtracting the total defect density rather than only the neutral defect density from the initial precursor density.

With the reaction enthalpy $\Delta H = F_0 - E_g$, due to the energy F_0 to form a neutral defect and the gain in gap energy E_g by e-h recombination, with the change in entropy $\Delta S = k(\ln 2 - \ln N_c N_v)$ given by the degeneracy of the neutral db and free carriers, and with the equilibrium carrier density $n_0 p_0 = N_c N_v exp[-E_g/kT]$, Eq.(1) may be expressed as

$$\frac{N_D}{N_t - N_D} = \frac{np}{n_0 p_0} \frac{2}{f^0} exp\left(-\frac{F_0}{kT}\right) \qquad (2)$$

N_D is larger by $2/f_0$ compared to a defect density obtained if no electronic reoccupation were allowed to take place. The physical mechanism responsible for the larger N_D is a depletion of created neutral defects on the right-hand side of the chemical reaction by subsequent capture or loss of an electron. It requires the conversion of additional precursors to maintain the equilibrium determined by the law of mass action between precursors and neutral defects, and therefore increases the total number of defects.

If the available sites where a defect state may be created have a statistical distribution with the probability P(E), from Eq.(2) the spectral shape of the defect structure is obtained

$$D(E) = \frac{np}{n_0 p_0} exp\left(-\frac{F_0}{kT}\right) P(E) \left(\frac{2}{f^0}\right) \qquad (3)$$

If F_0 is independent of E, the spectral shape is determined by the last two terms. The neutral occupancy is $f_0(E,E_f,U) \approx 1$ in the range $[E_f-U,E_f]$ and tails off exponentially outside. If P(E) is a Gaussian of width σ, the product $P(E)(2/f_0)$ shows a spectral shape that can be separated in 3 Gaussians, a centerband located at the pool position Ep and two sidebands at $E_p \pm \sigma^2/kT$. The physical mechanism producing the two sidebands is the mentioned depletion of created neutral defects by reoccupation. Because this depletion occurs selectively outside the range $[E_f-U, E_f]$, it causes formation of additional defects preferably below E_f-U and above E_f. These sidebands are a general result of electronic reoccupation during structural equilibration, and are independent of the details regarding the chemical reaction and formation energy. F_0 may for example include electronic contributions due to the difference in energy between the defect state and the wb state, $F_0 = F_{00} + (E-E_t)$. In such a case the same spectral shape for D(E) is obtained as above, but shifted by σ^2/kT to lower energies. We may further assume an exponential distribution of wb-energies, $g(E_t) = N_{vo} \exp(-E_t/kT_v)$. If each wb produces two db's at independent energy positions in the gap, a differential treatment applying the law of mass action between each slice of wb's at E_t and each slice of defects at E_1 and E_2, is required. The result is very similar to Eq.(3), only the center band is now located at $E_p - \sigma^2/2kT_v$, and the two sidebands shifted by $\pm \sigma^2/2kT_v$. Under non-equilibrium conditions, the enhancing factor due to the np-product turns out to be smaller than in Eq.(3). Involvement of Si-H bonds in the conversion process may further affect D(E), but the essential feature of the two sidebands remains.

In order to test the predictions of the defect poll model analysis we have measured light-induced ESR. Fig. 1 shows LESR absorption derivative spectra obtained from a 15μm film on a Cr-coated substrate. The four spectra were taken at excitation intensities and temperatures giving roughly an order of magnitude variation in the hole density, decreasing from $p_t = 3 \times 10^{17} \text{cm}^{-3}$ for the top spectra to 5.4×10^{16} for the bottom one. For better comparison, all curves have been rescaled to give equal amplitudes for the hole (h-) lines. Even casual inspection of line heights shows that, as the hole density drops, the electron density drops faster, indicating a distinct disproportionality between electron and hole densities.

Accurate values for electron and hole densities at the various excitation conditions were obtained by fitting the derivative spectra as well as the integrated absorption spectra with a superposition of two Gaussians. All lines for a given
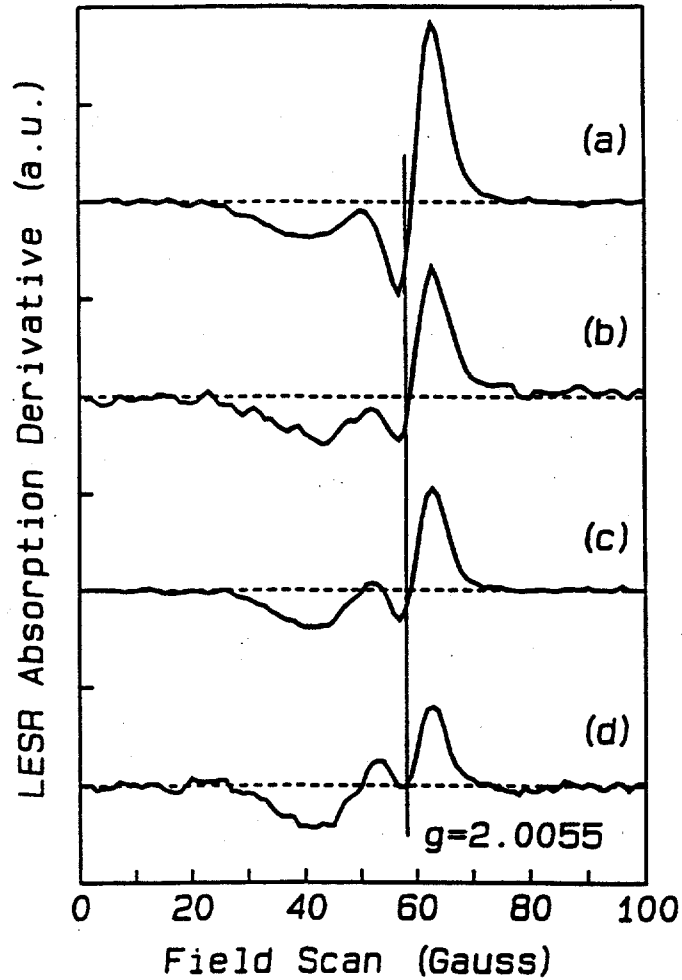
Fig. 1: LESR derivative spectra of an undoped 15μm a-Si:H film for various illuminations and temperatures. a) T=32K, microwave power P=8μW, white Light, p_t=3.3x10^{17}cm^{-3}. b) T=32K, P=8μW, residual signal after illumination, p_t=8.8x10^{16}cm^{-3}. c) T=95K, P=125μW, white Light, p_t=7.8x10^{16}cm^{-3}. d) T=95K, P=125μW, red light, p_t=5.2x10^{16}cm^{-3}. The spectra have been adjusted to give equal amplitudes for the hole lines.

temperature and different excitation energies were fit with one set of parameters for the line width and position, allowing only the line heights to vary. The line width and position change little with temperature and the hole and electron absorption could be determined with less than 10% relative error. Once the linewidth of the h-line is known, the ratio of the e- to h-line intensity can be directly read from the derivative spectra with good accuracy according to the relation

$$\frac{[h\text{-}line]}{[e\text{-}line]} = \frac{I_{pt}}{I_{nt}}x\left(\frac{\Delta H_{pt}}{\Delta H_{nt}}\right)2 \qquad (4)$$

4

where I_{pt}, I_{nt} are the line heights and ΔH_{pt},ΔH_{nt} are the peak-to-peak widths of the hole and electron derivative spectra, respectively.

The data of Fig.1 were taken for an intermediate light-soaked stage of the sample corresponding to a dark spin density $N_s = 1.1 \times 10^{16} cm^{-3}$. Similar changes in the spectra have been found in the annealed sample with $N_s = 3.2 \times 10^{15} cm^{-3}$ and after light-soaking to $N_s = 3.2 \times 10^{16} cm^{-3}$. Fig. 2 summarizes these results. Up to the
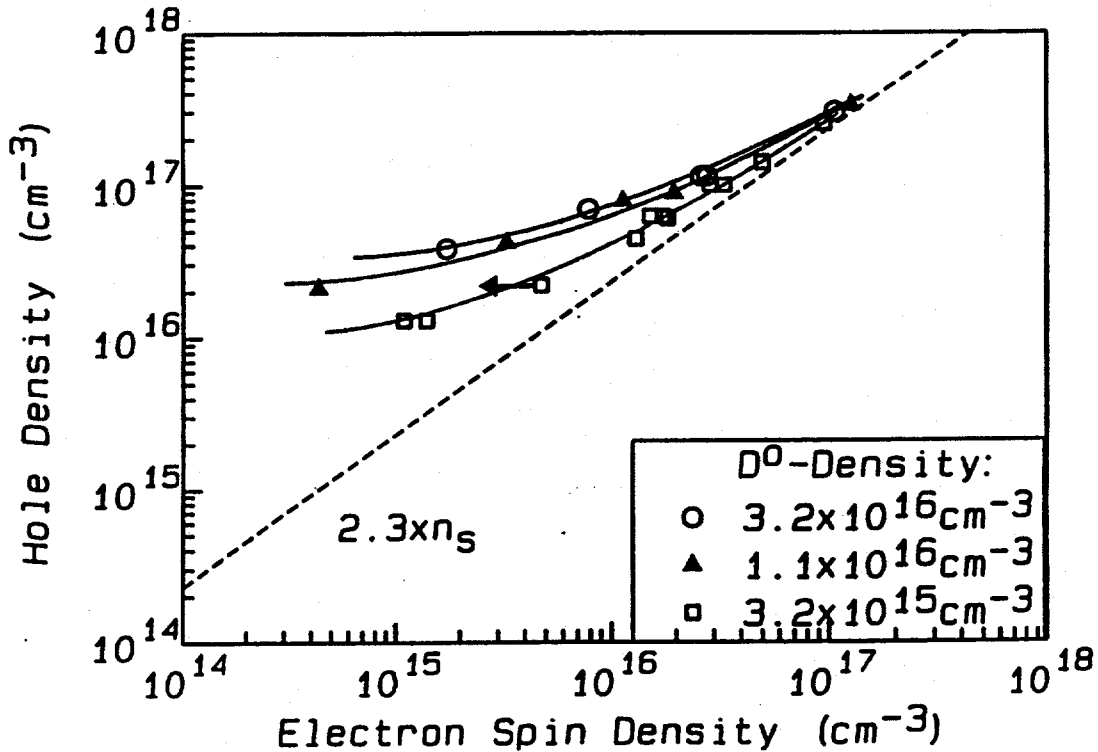
Fig. 2:Hole density vs. electron spin density n_s of the 15µm sample in the annealed and two light-soaked states with indicated dark spin densities, for various excitation intensities and temperatures.

highest intensities the hole density is larger than the apparent electron density, n_s, with a clear deviation from proportionality towards lower densities. At high intensities all data seem to approach proportionality with $p_t \approx c_1 \cdot n_s$, where $c_1 \approx 2\text{-}2.5$ and n_s is the electron spin density.

At sufficiently high excitation intensity, where the carriers trapped in the band tails dominate the total charge, charge neutrality requires an equal number of band tail electrons and band tail holes, $p_t \approx n_t$. A number of possible effects may contribute to the apparent lower electron spin density, n_s, compared to the total

electron density, n_t. One reason may be the rather small correlation energy of conduction band tail states leading to spin-coupling of the band tail electrons, as inferred from the temperature-dependence of the electron line in n-type material. In this case, only a temperature-dependent fraction of singly occupied tail states, n_s, is observed where the total number of electrons is $n_t = c_1(T){\cdot}n_s$. Fig.3 shows a normalized plot of $n_s(T)$ measured on a powder sample of phosphorous-doped a-Si:H deposited at 10^{-4} gas phase doping level, together with the calculated fraction
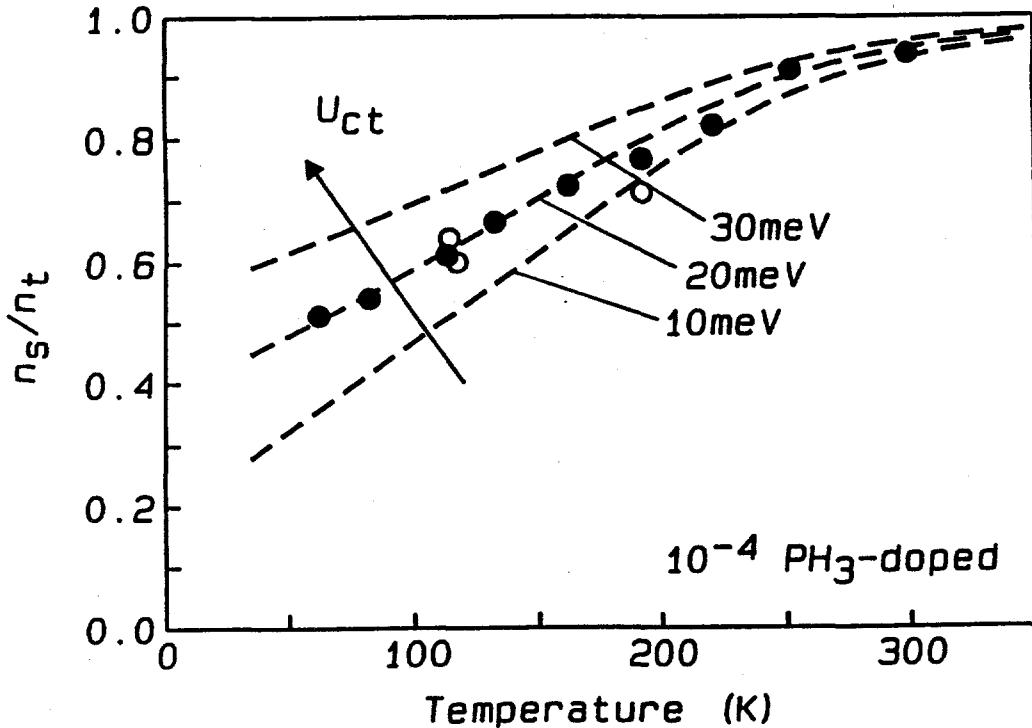
Fig. 3:Temperature-dependence of the normalized electron spin density for a lightly doped powder sample, and calculated fraction of singly occupied conduction band tail states assuming an exponential tail slope of 25meV and correlation energies $U_{ct} = 10$-30meV.

of unpaired electrons in thermal equilibrium, assuming conduction band tail correlation energies between 10meV and 30meV and an exponential conduction band tail slope of 25meV. The data suggest a correlation energy of about 20meV, which yields $c_1(T) = 2.3$ at 32K, in agreement with the proportionality constant inferred from our LESR measurements. Of course, other combinations of tail slope and correlation energy give similar fits, but the effect on $c_1(T)$ in the temperature range of interest is very small and does not affect the LESR results derived in the following. For doping levels of 10^{-2} and above, deviations from the monotonic increase of n_s with T are found. The origin of these deviations is unclear, but increased coupling with dopant states might be a reason.

Taking $c_1(T)$ of Fig. 3 into account, the total electron density, $n_t = c_1 \cdot n_s$, approaches p_t at high excitation intensities. However, a marked difference $\Delta N = p_t - n_t$ still exists at lower intensities. ΔN is nearly constant over 2 orders of magnitude change in n_t, indicating the presence of additional, negatively charged defects, $N_{D-} = \Delta N$ to compensate the charge of the excess hole density. A slight increase of these charged defects from 2×10^{16} to 4×10^{16} and 5×10^{16} cm^{-3} is observed when degrading the sample from a dark spin density of 3×10^{15}cm^{-3} to 1.1×10^{16} and 3.2×10^{16}cm^{-3}, respectively. The corresponding ratio of charged to neutral defects, $\Delta N/N_s$, decreases from about 7 in the annealed sample to 4 and 1.6 in the two light-soaked states. In the range of large n_t and p_t the derived difference ΔN is sensitive to the exact value of c_1. However, towards smaller n_t, where most of our data are taken, the influence of c_1 on this difference becomes marginal, and the derived ΔN is quite accurate. In Fig.3, due to the log-log scale over 4 orders of magnitude, the deviation from proportionality may not appear significant in the medium range, where $n_s \approx 10^{16}$. However, this is the range corresponding to Fig.1b,c where the ratio of h- to e-line intensities increases from 2.3:1 to about 3.5:1 - 5:1, indicating deviations from proportionality by up to 50%. The range of lowest n_s, corresponding to Fig.1d, shows ratios in excess of 9:1.

Our LESR measurements show a distinct deviation from proportionality between band tail electron and hole density as well as a small positive LESR signature of the db-line in the bulk of undoped low defect a-Si:H. The results suggest a density of charged dbs which is at least a factor 5 higher than the density of neutral dbs. Occupancy calculations confirmed that under illumination most dbs become negatively charged, and therefore no appreciable positive LESR signature of the db-line is expected, even for a dominant fraction of charged dbs present in the dark.

2. The effect of post-deuteration on metastability in a-Si:H

While the effects of hydrogen introduced during film growth on the equilibrium defect density, metastability and the Si-Si bond disorder in a-Si:H have been widely studied, little is known about the influence of additional hydrogen or deuterium induced in a remote plasma after the sample preparation. We therefore examined the effect of post-deuteration on the equilibrium and metastable defect properties of a-Si:H. Hydrogenated amorphous silicon films were deuterated through a sequence of 1h exposures to a remote deuterium plasma at 350°C. The concentration

profiles of hydrogen and deuterium were determined by SIMS at various times during the exposure sequence. The defect density was determined using CPM.

Typical concentration profiles of post-deuterated a-Si:H films obtained after 1 and 8 hours exposure to monatomic deuterium are represented in Fig. 4. At the sample surface H is displaced by the introduction of deuterium. The hydrogen loss at the surface varies between a factor of 10 and almost two orders of magnitude after 1 and 8h of deuteration, respectively. With increasing deuteration time, t_D, the H displacement extends to the interface indicated by the peaks in the concentration profiles (Fig. 4b). The H diffusion length is the same for hydrogen out-diffusion and
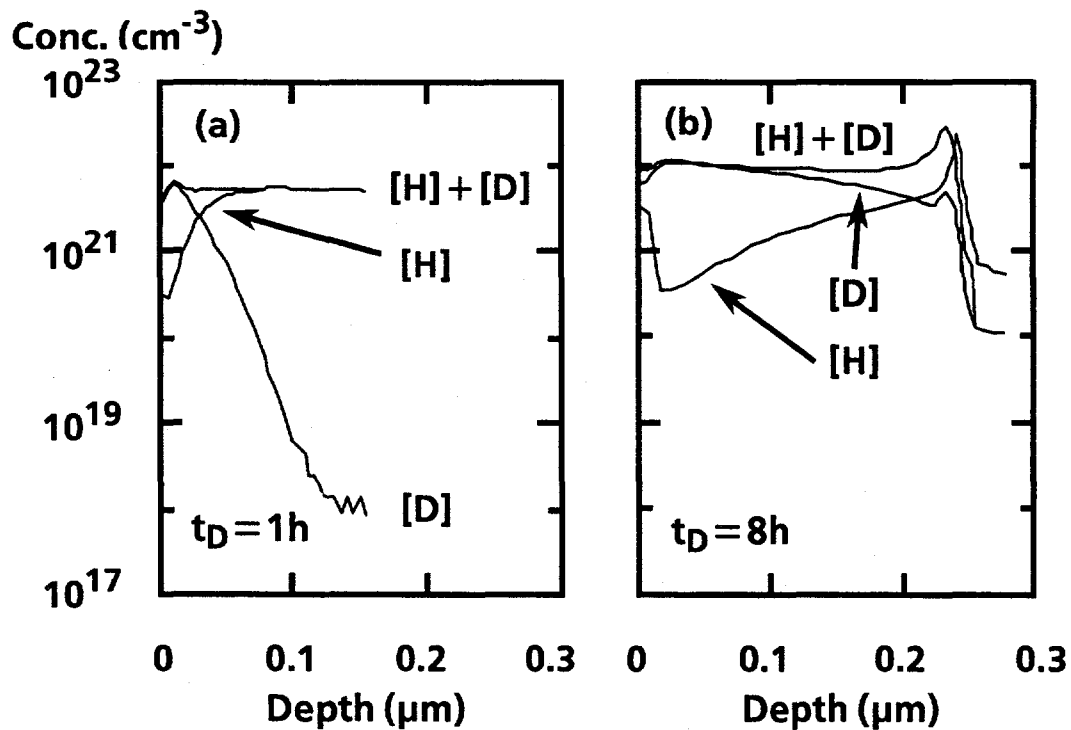
Fig. 4: Hydrogen and deuterium depth profiles of a-Si:H films after $t_D = 1h$ (a) and 8h (b) exposure to a remote deuterium plasma at $T_D = 350°C$. The peak in the profile indicates the interface to the substrate.

deuterium in-diffusion indicating that D and H have the same diffusion coefficients. In addition to the displacement the total concentration of hydrogen and deuterium, [H+D], increases from $5 \times 10^{21} cm^{-3}$ to $1 \times 10^{22} cm^{-3}$ at $t_D = 8h$. Raman measurements performed on post-deuterated a–Si:H revealed that deuterium is bonded to Si atoms and with increasing D concentration. This is in good agreement with the SIMS results of Fig. 4. Deuteration not only replaces hydrogen by deuterium atoms, but

also increases the Si-D bond density. This, however, chould have a direct influence on the defect density, N_D, and on the metastability of amorphous silicon.

Figure 5 shows CPM spectra at 300K measured in the annealed state and after light soaking for 15.5hr. The solid curves represent the initial *as-deposited* a-Si:H films ($t_D = 0$h). The dashed and dotted curves were obtained after 3 and 6 hours post-deuteration at $T_D = 350°C$, respectively. Since an exposure to monatomic deuterium for 8 hours did not change the Tauc-gap determined from transmission measurements the CPM spectra obtained from post-deuterated samples were normalized to the band tail region at the $t_D = 0$h sample. Thus the CPM signal is increased by a factor of 2 at $h\nu \geq 2$eV which presumably is related to a change in the surface band bending of the film. In both, the annealed and the light soaked states, neither the Urbach-slope nor the defect region ($h\nu = 0.8$ to 1.3eV) changes with an increase of the total H+D concentration. This result indicates that the additional deuterium neither increases the defect density, N_D, in state A, passivates preexisting dangling bonds nor decreases the weak bond density. Intense light soaking
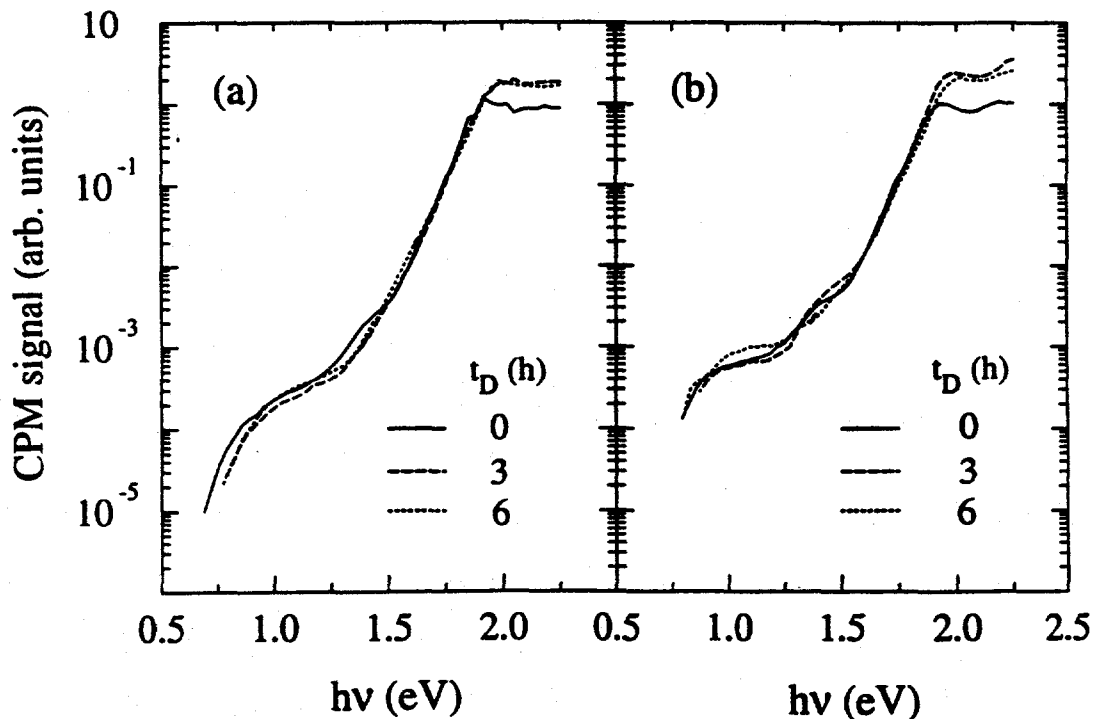
Fig. 5: CPM spectra of a-Si:H samples measured at 300K before and after exposures to monatomic deuterium from a remote plasma for 3 and 6 hours, respectively. (a) represents the annealed state and (b) shows the spectra after intense light soaking with white light ($P = 5$W/cm^2).

9

increases the defect density up to a factor of 3 indicating that the amorphous network is not stabilized by increasing the total H+D concentration.

In Figure 6 the increase of the defect density, ΔN_D, is plotted as a function of the deuteration time, t_D (full circles). The values were obtained by taking the ratio of the CPM spectra in state A and state B. Independent of the H+D concentration light soaking creates $5 \times 10^{16} cm^{-3}$ dangling bonds. Furthermore, E_C-E_F in the annealed state and after degradation was determined and plotted as a function of t_D. The variation of E_C-E_F with t_D is consistent with an increase of the CPM signal at $h\nu \geq 2eV$ after post-deuteration. In thin films ($d=2500\text{Å}$) surface band bending has a large influence on E_C-E_F. Post-deuteration ($t_D \geq 2hr$) obviously reduces the band bending resulting in an increase of the Fermi level of about $0.1eV$. E_C-E_F obtained after light soaking shows the same dependency on t_D as in the annealed state. Furthermore, the increase of E_C-E_F of $0.1eV$ due to the illumination is independent of the total H+D concentration consistent with the concentration independent defect creation.

Fig. 6: Fermi energy before (squares) and after illumination (triangles) and the change of the defect density, ΔN_D, (circles) as a function of the deuteration time, t_D. The a-Si:H films were illuminated with white light at 300K for 15.5 hr.

Post-deuteration of a-Si:H does not alter the defect density in state A, change the Urbach edge, nor significantly alter metastable defect formation, and the light-induced increase in the defect density is independent of the total H+D concentration. These results sugg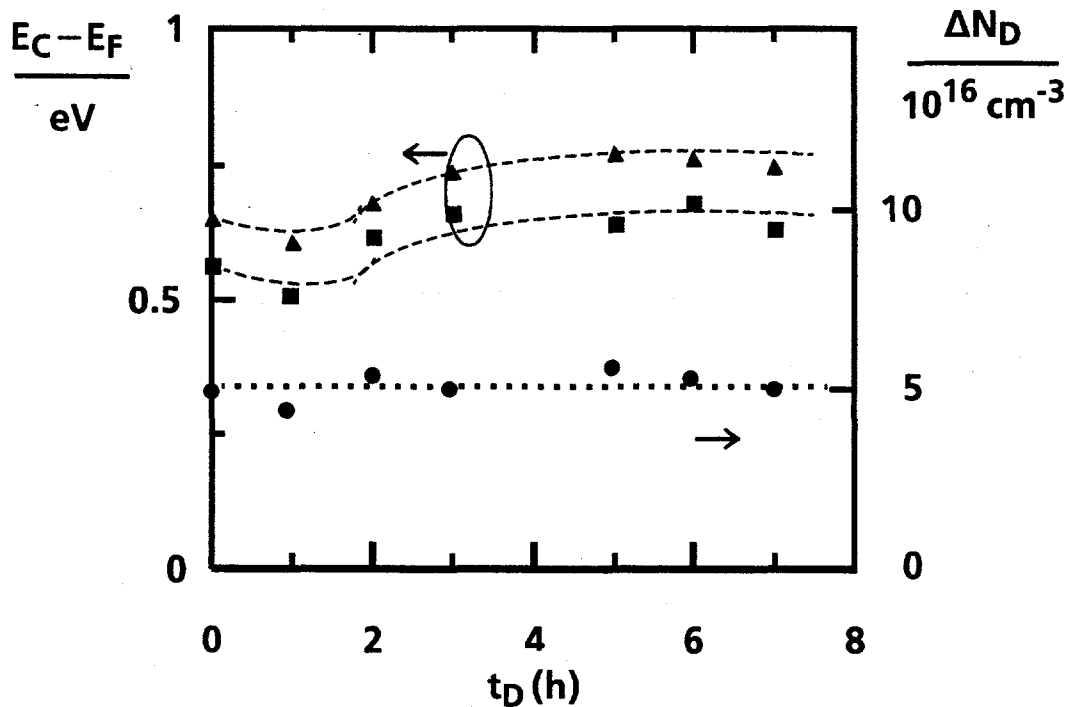est that deuterium always enters the sample in pairs pinning the hydrogen chemical potential μ_H, which supports the idea of a negative U system for hydrogen and deuterium. Because the increase of Si-H bonds did not change the annealed dangling bond density or the weak Si-Si bonds responsible for the band tails, these results suggest that the density of weak Si-Si bonds is determined by equilibration with strong Si-Si bonds through the interchange of H just as the dangling bond density is determined through thermodynamic equilibration between dangling bonds and weak bonds.

3. Kinetics of small changes from equilibrium

The origin of the non-exponential kinetics of metastable defect generation and annealing is an important unresolved problem. Possible causes of non-exponential behavior are the time dependence of the rates of creation and annealing, and a distribution of reaction rate constants. We have examined thermal quenching metastability in doped materials for small changes from equilibrium by experiment and numerical simulation. Details of the calculations are given in section B2 and the comparison between experiment and data are discussed here. The relaxation kinetics of 10^{-3} and 10^{-4} P doped a-Si:H due to small changes in temperature have been measured using conductivity of samples immersed in various oil baths. The sample reaches equilibrium in one oil bath at temperature T_A and is then rapidly immersed into a stirred temperature controlled bath at temperature T_M. The conductivity is measured as the sample equilibrates at the new temperature. The change in conductivity has been shown to be proportional to the change in the number of activated dopants.

The relaxation exhibits a stretched exponential time dependence

$$\Delta(t) = \Delta(0)\, exp\left[-\left(t/\tau \right)^{\beta} \right] \tag{4}$$

where $\beta \leq 1$, τ is the time constant, and $\Delta(0)$ is the initial deviation from equilibrium. The kinetics are exponential only if $\beta \approx 1$. In Fig. 7, the measured and simulated value of τ for two fixed measurement temperatures (T_M = 383 and 416K) as T_A is

11
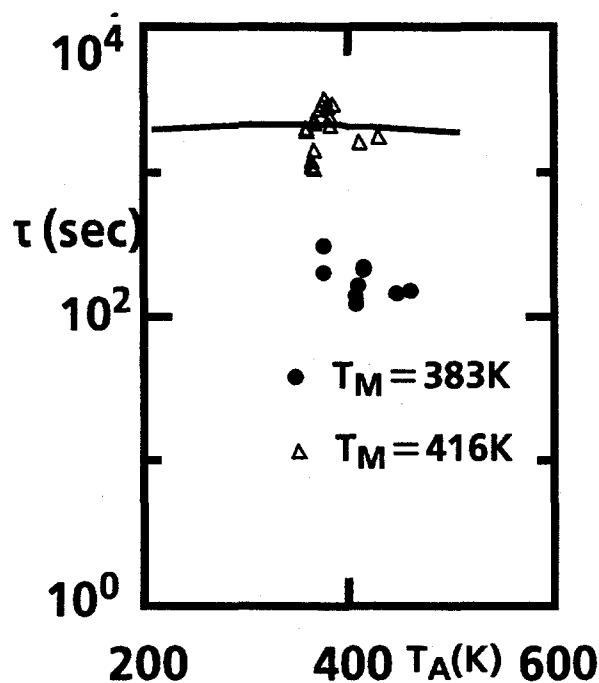
Fig. 7 τ as a function of T_A for the indicated measurement temperatures. The line presents the results for the distribution of sites and energy barriers model.
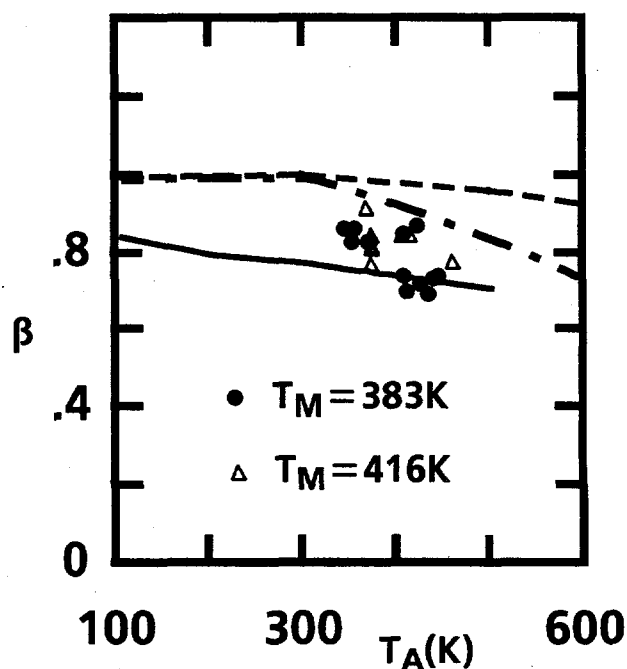
Fig.8 The dispersion parameter vs. initial temperature, T_A for the indicated measurement temperatures. The solid line shows the dispersion for the simulation of a distribution of site and barrier energies while the dashed line represents the behavior for a distribution of sites communicating with a single extended transport level. The dot-dashed line indicates the initial slope of the decay for this model.

varied from below to above T_M does not exhibit any significant variation with annealing temperature. As a function of T_M however, there is a significant variation of τ; it is activated with an energy of 1.1 eV In Fig. 8, the values of β are plotted. Even for changes as small as 5°C, the kinetics deviate significantly from an exponential. β is no larger than 0.85 and and can be as small as 0.6. Therefore, we can conclude that the dopant passivation process is not solely a function of the dopant or carrier density. Therefore, two samples with the same carrier density may exhibit different decays depending on previous history and/or population of various distributions. Finally, in Fig. 9, the change in the carrier concentration divided by the equilibrium carrier concentration $\Delta(0)/N_{eq} = [N(0)-N_{eq}]/N_{eq}$ is plotted versus T_A. For $\Delta E/k > > T_A$, this ratio approaches $exp[\Delta E (1/kT_M - 1/kT_A)]-1$ where ΔE is the carrier formation energy. Fitting the ratio to this form, we can conclude that the carrier
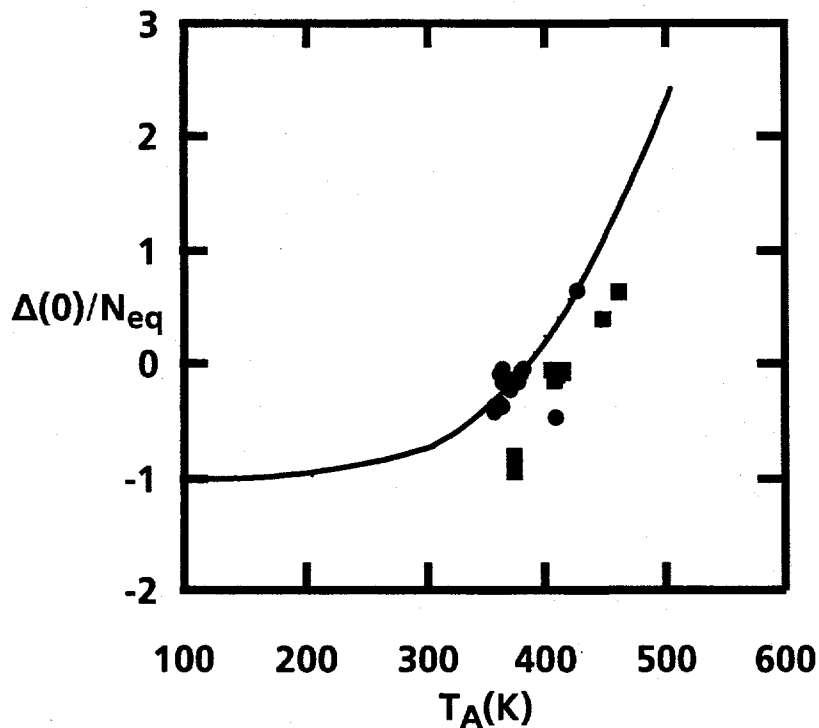
Fig. 9 The total change in carrier concentration divided by the equilibrium carrier concentration for the indicated measurement temperatures. The line represents the results of a simulation with a distribution of barriers and sites.

formation energy is about 0.2 eV and the corresponding dopant formation energy is about 0.02 eV. For such small changes in disordered materials, one expects a small formation energy since there is always a small number of defects near zero formation energy. By comparing these results with simulations, we can draw additional conclusions about the characteristics of the metastable mechanism discussed in the section B2.

4. Comparison of current and light induced defects in a-Si:H

Both prolonged illumination and a forward bias current cause a metastable increase in the defect density of a-Si:H and the degradation of p-i-n solar cells. There is good reason to expect that the same defects are formed because both mechanisms generate electrons and holes which cause defect creation by recombination. However, there have been a few suggestions that current-induced and light-induced defects are different. We therefore performed experiments and numerical modelling which compare defect generation by illumination and forward current on the same sample. Measurements were made of the subgap absorption and of the reverse bias current, both of which yield a measure of the defect density.
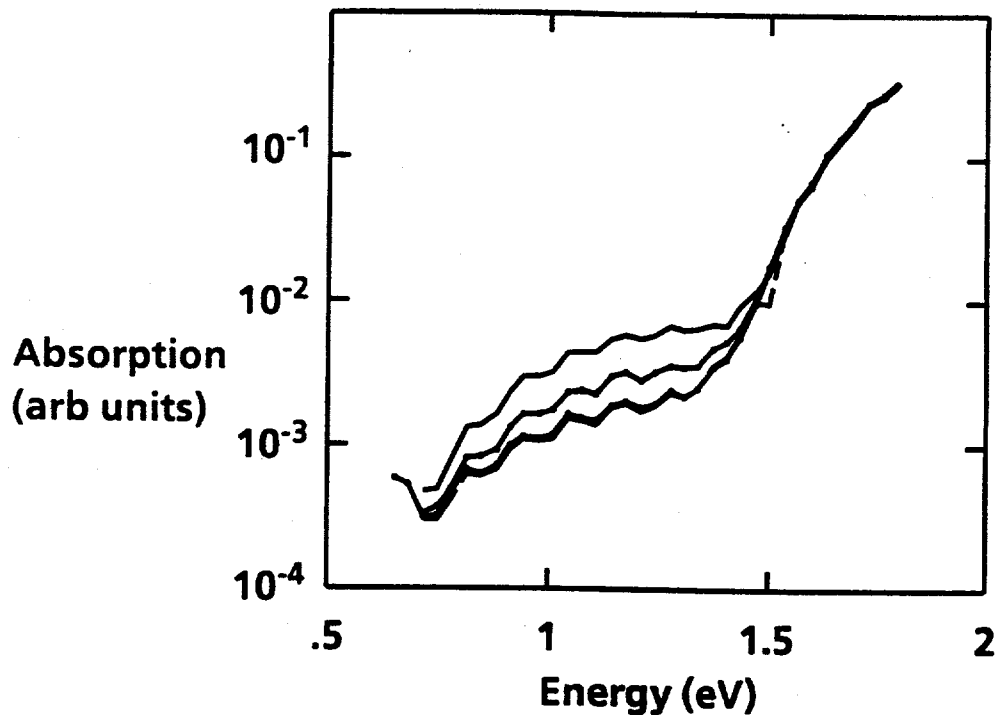
Fig 10. CPM data showing the increase of the sub-gap absorption after current-induced defect formation. The Urbach edge region is unchanged.

Figure 10 shows examples of the CPM data for a sample in the annealed and various current-soaked states. The sub-gap absorption increases after defect generation and the Urbach edge slope is unchanged, as found for the light-soaked samples. There is an order of magnitude increase in the defect density as compared to the annealed state, which is typical of other degradation measurements. Differences in the shape of the defect absorption bands were investigated by taking ratios of subgap spectra. Within the uncertainty of the measurements, the absorption band is identical for the two types of defect creation mechanisms, indicating that there is no difference in the gap state energy levels of the defects.

The room temperature reverse bias current decreases after the voltage is applied, eventually reaching a constant value after 5-10 minutes. The data show that both light soaked and current soaked samples have a higher reverse current than the annealed state, and the form of the current decay is the same for both defect creation mechanisms. This confirms that defect creation occurs with both mechanisms and again indicates that the defects are the same. However, the reverse bias current-voltage (J-V) characteristics for the annealed and defective states are shown in Fig. 11 and clearly reveal a difference in the two defect generation

14
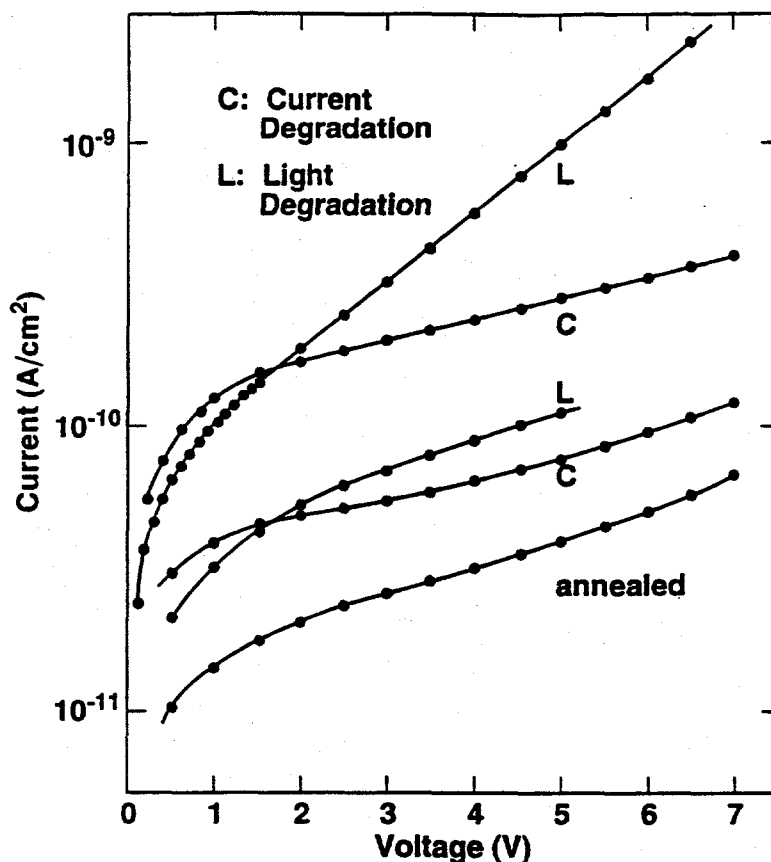
FIGURE 11. Reverse bias current-voltage (J-V) characteristics of a p-i-n diode after various stages of light and current induced defect generation, as indicated.

processes, particularly when the defect density is large. Light induced defects result in a current which is smaller at low bias, but increases more rapidly than for the current induced defects.

Figure 12 plots the relative magnitude of the subgap absorption and the reverse bias generation current measured at 1V. Overall a linear relation is observed, consistent with the same defects being present. However, the light-induced defects fall on a different line from the current-induced defects. In both cases, the CPM measure of the defect density is proportional to the reverse bias measure, but the light-induced defects have a 50-100% higher absorption for the same reverse current. This difference is consistent with the results of Fig. 11, since at 1V bias the current in light soaked samples tends to be small. Approximate linearity for each type of defect mechanism occurs because the J-V data are roughly parallel.

15
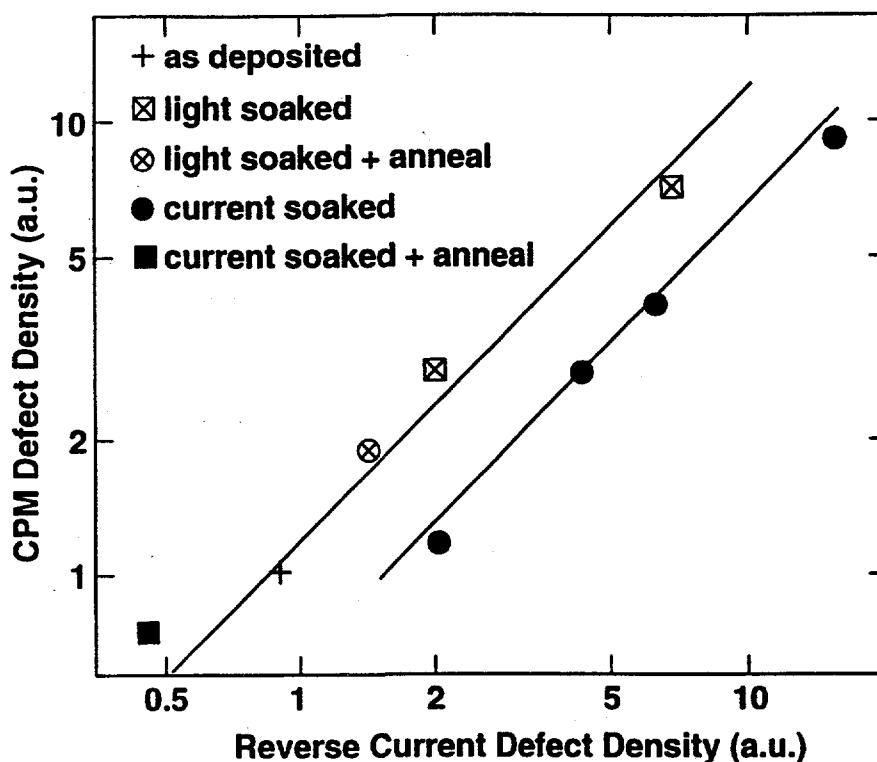
FIGURE 12. Plot of the relative defect densities obtained from CPM and reverse current measurements showing linear behavious but with an offset between the two types of defect creation.

However, the departure from linearity at low defect densities is probably due to a slight change in shape of the J-V data.

We conclude from the results that light and current soaking result in generally identical defects with the same gap states. However, differences exist which are manifested in the reverse J-V data. The shape of the J-V data is governed by the electric field dependence of the thermal generation and contact injection components of the current. Numerical modelling was therefore used to study the J-V characteristics and is described in the next section. The results indicate that light soaking introduces a high density of defects close to the p-i interface while current soaking gives a more uniform distribution. This conclusion agrees with the expected physical situation since a forward current injects electrons and holes from opposite sides of the sample, while light absorption creates electrons and holes in the same location with a concentration that decays exponentially from the illuminated contact. Recombination therefore creates the highest metastable defect density near the illuminated contact.

16

B NUMERICAL SIMULATIONS

Numerical simulations of measurements are a critical aspect of research in a-Si:H, because analytical models usually require severe approximations which limit the accuracy of the solutions. We perform simulations of electrical transport and hydrogen diffusion and metastability.

1. Modelling of the reverse current in p-i-n diodes

Electrical transport in p-i-n diodes are simulated with a numerical model which is a two dimensional solution of Poisson's equation together with the electron and hole continuity equations. The density of states in the gap is represented by 34 trap levels spaced by 50 meV giving a band gap of 1.72 eV. Parameters for the carrier mobilities, capture cross-sections, band tails etc. are the same as have been used in previous modelling studies. We have applied the modelling to the reverse bias studies of metastable defects and have investigated whether a different spatial distribution of defects could explain the J-V characteristics observed before and after defect creation. The reverse current in a-Si:H p-i-n diodes has components arising from bulk thermal generation or contact injection, and calculations for these two mechanisms are given below. The defects influence the field through the depletion charge, and the field affects the reverse current.

The thermal generation current, J_{th}, corresponds to the excitation of electrons and holes from defect states near mid gap and is given by,

$$J_{th}(V) = N(E_{FD})kT\, P(E_{FD})\, \xi(F)\, \Omega \tag{5}$$

where E_{FD} is the defect quasi-Fermi energy, N is the density of states, P is the thermal excitation rate, ξ describes the field (F) dependence of the excitation rate attributed to lowering of the energy barrier, and Ω is the sample volume. The field dependence is simulated by a Poole-Frenkel model for the field-dependent emission rate, having the form,

$$J_{th}(F) = J_{th}(0)\, exp[\beta_1 F(x)^{1/2}] \tag{6}$$

where x is the position in the sample. A spatially varying distribution of defects is simulated by dividing the sample up into three regions; regions 1 and 3 extend 0.2 µm from the p and n contacts respectively, and region 3 is the central 0.8 µm of the

1.2 µm device. The defect density in each region is increased by a specific factor, usually chosen to be 10 or 30. The undegraded material has a total defect density of about 3×10^{15} cm^{-3}.

Calculations of the field dependence of the thermal generation are shown in Fig. 13. Curve 1 is the simulated current for the undegraded sample with β_1 chosen to give a J-V curve which agrees with the data in Fig. 11. Curve 2 shows that a uniform increase of the defect density increases the current, but with little change in the field dependence. Curve 3 shows the effect of concentrating the defects near the p-i interface, by increasing the defect density in region 1 by a factor 30, but leaving the rest of the i-layer undegraded. The current is large, the field dependence below 1.5V is strong, but above 1.5V the field dependence is weaker than for uniform degradation. We explored other combinations of parameters but were unable to simulate the strong field dependence of the current after light degradation.
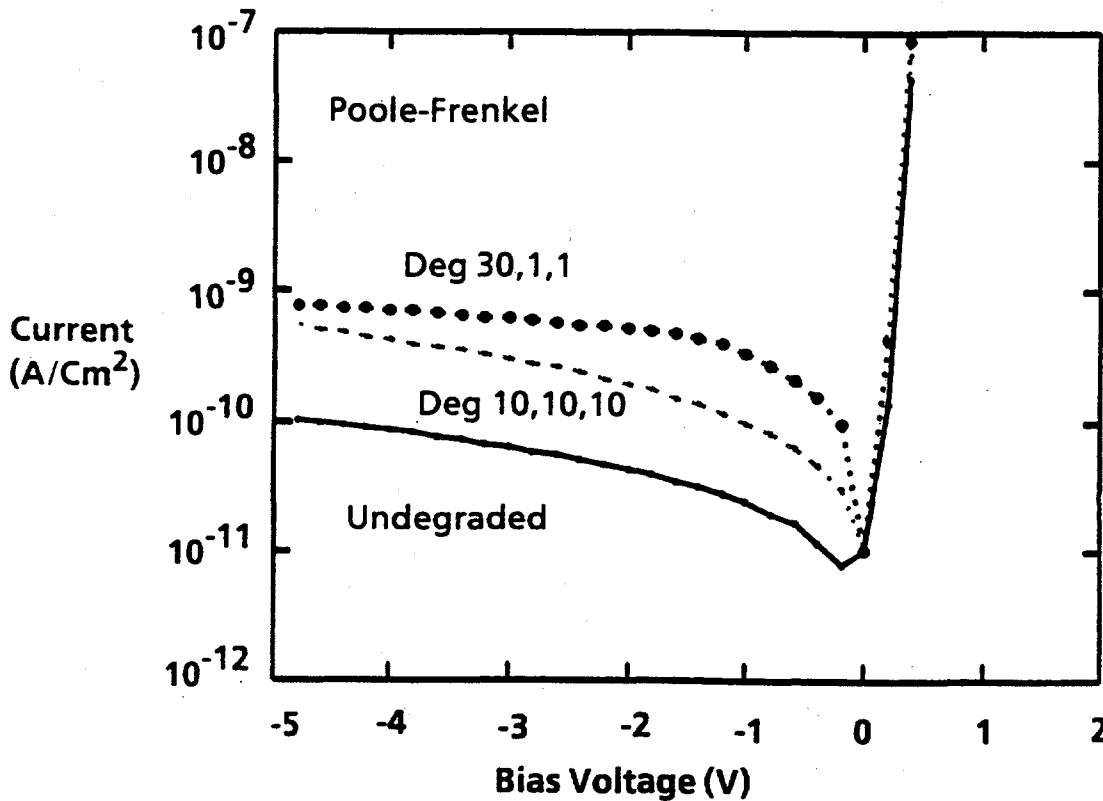
FIGURE 13. Numerical calculation of the J-V characteristics assuming a Poole-Frenkel enhancement of the thermal generation current, and no contact injection. The assumed degradation factors of the three regions of the sample are shown.

The contact injection curent is modelled as tunneling from the Fermi energy of the doped layer to the band edge of the i-layer. The tunneling distance is roughly E_B/F_C, where E_B is the energy barrier and F_C is the electric field at the contact. The injection current should therefore be given by,

$$J_{inj}(V) = const. \; exp[\, -2E_B/F_C(V)R_o] = const. \; exp[-\beta_2/F_C(V)] \qquad (7)$$

where R_o is the electron localization length. Figure 14 shows calculations of the current when the contact injection term is included but the Poole-Frenkel enhancement of the thermal generation current is removed. The undegraded sample exhibits a low current and little field dependence because the current is dominated by thermal generation. Curve 2 shows that a uniform degradation by a factor 10 increases the field dependence slightly. Curve 3 shows that when region 1 near the p-contact is degraded by a factor 30, the current is much larger and increases exponentially with the field in reasonable agreement with the slope of the
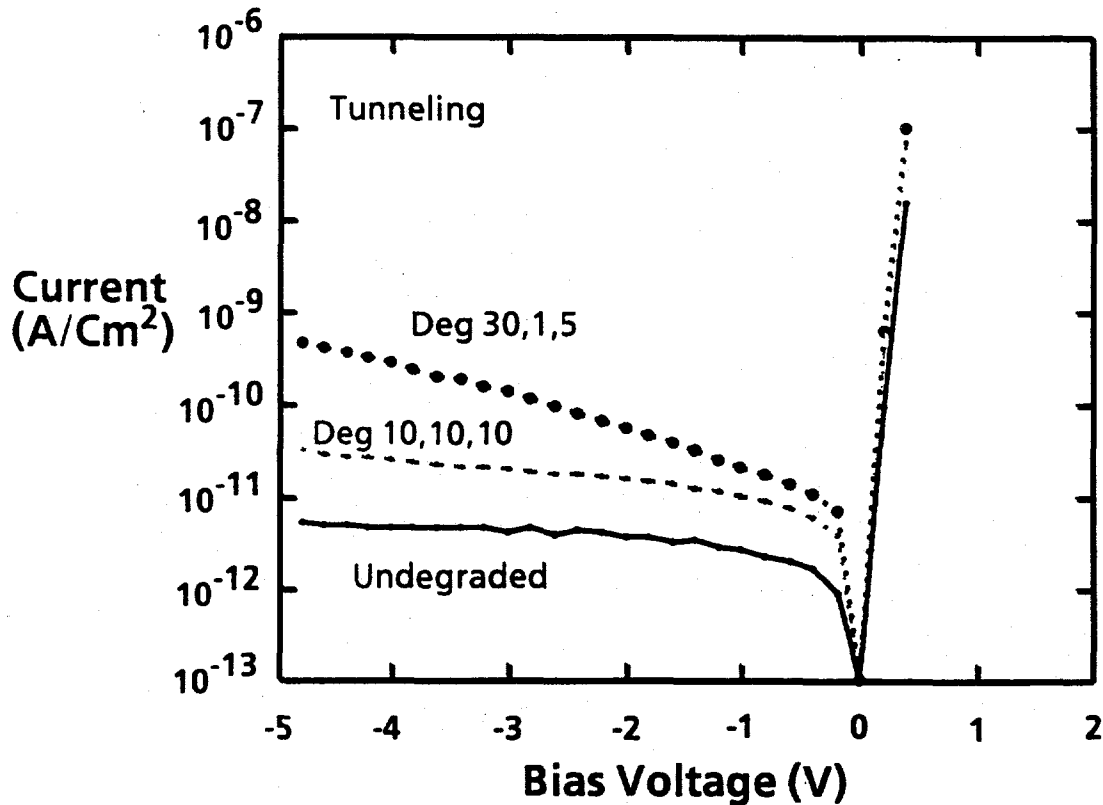

FIGURE 14. Numerical calculation of the J-V characteristics assuming a tunneling enhancement of the injection current. The assumed degradation factors of the three regions of the sample are shown.

light soaked sample in Fig 11. The contact injection data are fitted with a value of β_2 of about 3×10^6 cm/V. From eq. 3 this corresponds to a localization radius of 15Å for an energy barrier of 0.5 eV.

Our results show that the same dangling bond defects are created by illumination or by a forward bias current in p-i-n diodes. However, light soaking introduces a high density of defects close to the p-i interface while current soaking gives a more uniform distribution. This conclusion agrees with the expected physical situation. A *forward* current injects electrons and holes from opposite sides of the sample, and their concentration decreases with distance from the injecting contact due to recombination. The metastable defect density depends on the local recombination rate which is reasonably uniform, but with a broad maximum in the middle of the sample. In contrast, light absorption creates electrons and holes in the same location with a concentration that decays exponentially from the illuminated contact. Recombination therefore creates the highest metastable defect density near the illuminated contact.

2. Simulations of hydrogen-induced metastability

We have simulated the dopant equilibration data described in section A3. Consideration of small changes from equilibrium greatly simplify the analysis of the kinetics. For example, in the case of a model which depends on the concentration of a single species such as the dopant or carrier concentration, the change in concentrations can quite generally be written as

$$\frac{dN(t)}{dt} = f(N(t)) \tag{8}$$

where f is some general function including the effects of defects on carrier density etc. For small changes about the equilibrium values N_{eq} defined by $f(N_{eq})=0$, we can expand f using Taylor's theorem yielding

$$\frac{d\Delta(t)}{dt} = \frac{\partial f}{\partial \Delta} \Delta(t) = -R\Delta(t) \tag{9}$$

where $\Delta(t) = N(t) - N_{eq}$. The time dependence of such a system should therefore be exponential.

On the other hand, if f depends explicitly on the time, then for small changes the time dependence will not be exponential. Alternatively, if there a number of

parallel processes enumerated by a variable such as the barrier energy, E, the time decay of the system is determined by

$$\frac{d\Delta(t,E\ )}{dt} = -R(E)\Delta(t,E) \tag{10}$$

assuming that the processes run independently. The measured change in defects is given by

$$\Delta(t) = \int \Delta(t,E)\ dE = \int \Delta(0,E)\ e^{-R(E)\ t}\ dE \tag{11}$$

where $\Delta(0,E)$ is the initial change in concentration. The time dependence is not exponential in general, and if $\Delta(0,E)$ is exponential in E as is often the case since it is the difference between Boltzman occupation statistics of the sites at the annealing temperature, T_A and the measurement temperature, T_M, the time dependence is approximately stretched exponential even for very small changes from equilibrium. Thus, the important conclusion is that nonexponential kinetics for small changes from equilibrium indicate that the physics of metastability is not solely a function of only the concentration of some species such as carriers or dopants.

A number of models involving the motion of H have been proposed for dopant and defect metastability. One class of models supposes that only H on neighboring atoms passivate the dopants by a reversible process and there is no significant interchange of H between sites. As a result, the defects can be regarded as a distribution of independent two-level systems. A second class of models assumes that H resides in a distribution of trapping sites some of which are associated with dopants. Each trapping site can interchange H with a single transport state which can interchange H with all other sites. The third class of models consists of a distribution of trapping sites which can interchange H with neighboring sites over a distribution of barriers.

For the single transport level model, we numerically solve for the trap occupation probabilities N_i and [H] in the trapping and release equations

$$\frac{d[H]}{dt} = \sum_{i=1}^{n}\left[v_i\ N_i - 4\pi R_c\ D_H[H]\left\{ N_i^T - N_i \right\} \right] \tag{12}$$

21

$$\frac{dN_i}{dt} = -v_i N_i + 4\pi R_c [H]\left\{ N_i^T - N_i \right\} \quad i=1, n \tag{13}$$

with

$$v_i = V_0 \exp\left[-\left(E_c - E_i \right)/kT \right] \quad i=1, n \tag{14}$$

for a discrete series of trapping levels whose total concentration, N_i^T increases exponentially with decreasing energy, E_i until a cutoff energy E_τ according to $N_T/(kT_s) \exp[(E_\tau - E_i)/kT_s]$ where N_T is the total trap density, kT_s is the characteristic site disorder energy, R_c is the capture radius, and D_H is the interstial diffusion coefficient. When the H occupies the dopant site, the dopant is passivated, otherwise it is active. The time dependence of the active dopant concentration, mobile [H], and the occupation factors are computed as a function of time.

The results are close to a stretched exponential so the dopant curves were fit to Eq. (4). The resulting values of β are plotted in Fig. 8 represented a dashed line and a determination of β from the initial slope plot of $\log \Delta$ vs $\log t$ by the dot-dashed line. The important results are that for small changes around equilibrium, β approaches 1. For $T_A > T_M$, the initial rate β is approximately given by T_M/T_A and 1 for $T_A < T_M$. The results show that stretched exponentials and power law decays of effective reaction rates occur quite generally when the initial occupation is determined by exponential Boltzman factors. However, the results clearly do not agree with the data where $\beta \simeq$ 0.8 for small changes. The problem with the model where states communicate with a single transport level is that for small changes, there is only one time constant reflecting the time it takes to excite from the chemical potential to the transport level. The data clearly indicates a distribution of rate constants. Hence, we consider the third class of models.

The third class of models was investigated by solving the master equation

$$\frac{dn_i}{dt} = \sum_{i=1}^{n}\left[\omega_{i\leftarrow j} n_j\left(1-n_i \right) - \omega_{j\leftarrow i} n_i\left(1-n_j \right) \right] \tag{15}$$

for the occupation probabilities, n_i of a cubic block of sites ranging from 11^3 to 26^3 sites which can interchange H with 6 neighboring sites over an exponential

distribution of barriers, E_{ij} between site i and j. The transition probabilities $\omega_{i\leftarrow j}$ are given by

$$\omega_{i\leftarrow j} = v_0 \exp\left[-\left(E_{ij} - E_j \right)/kT \right] \tag{16}$$

The site energies, E_j were also selected to be exponentially distributed. The boundary sites communicate with opposing sides (wraparound transitions) to avoid boundary effects. Sites with energies in a given energy band were labeled as dopants, and the total unoccupied dopant concentration and total H concentration was determined as a function of time. Insuring that the total H concentration remained conserved over time, proved to be a good guide for insuring proper convergence. The time dependence of the dopant concentration was fit to Eq. (15), and the results are depicted as solid lines in Figs. 7-9. No attempt was made to find model parameters which fit the data most optimally.

In general, we see that the features of the data are captured by this sort of model. In particular the fact that β remains significantly less than 1 as T_A approaches T_M from above and below. The distribution of time constants in such a model insures that the kinetics remain nonexponential even for small changes. As shown in Fig. 7, τ is more or less independent of T_A, since the average barrier to reach equilibrium does not change for different equilibration temperatures. In most cases, increasing T_A results in H occupying slightly higher energy sites, reducing the average barrier and hence τ, which reflects the most probable barriers, decreases as well. The model also reproduces the dependence of $\Delta(0)/N_{eq}$ ratio on T_A in Fig. 9. A fit to this curve is obtained by insuring that the dopant energy level is about 0.2 eV from μ_H so that the formation energy is on this order.

It is important to note that the small value of β for small changes is not due solely to the presence of a distribution of barriers. Even for a single barrier height but a distribution of site energies gives rise to stretched exponentials within the simulations. The key feature is that a H atom can only sample neighboring sites. Therefore, in order to reach donors sits site some distance away, the H atom must visit a number of traps of different energy thereby experiencing a distribution of different hoping rate.

C. ELECTRONIC TRANSPOPORT

1. Hall measurements

The sign of the Hall effect measured on a-Si:H is electron-like (negative) for p-type doping and hole-like (positive) for n-type doping and intrinsic material. The sign reversal is characteristic of disordered semiconductors and seems to be a result of the very small scattering distance, but is still poorly understood. We explored Hall experiments on intrinsic, phosphorus- and boron-doped a-Si:H and on phosphorus-doped a-SiC:H with varying C-content. We compare the results with sweep-out experiments that give the band tail carrier density, n_{BT}, and DC-dark conductivity which together determine the drift mobility, μ_D, on doped a-Si:H.

A series of intrinsic, phosphorus and boron doped a-Si:H specimens, and some phosphorus-doped a-SiC:H alloys were prepared. The Hall measurements were made in vacuum with a cryostat optimized for Hall experiments on specimens deposited onto Corning 7059 glass. Cr contacts produced either by photolithography or by simply evaporating through a given mask in a four-electrode geometry (Van der Pauw) were covered with gold to reduce the noise level. Thin, 40 nm, highly-doped layers have been introduced in between the Cr and the amorphous semiconductor to create ohmic contact characteristics. Reliable values for the small Hall potential, U_H, in the range 5 to 40 µV were obtained by recording U_H from a series of magnetic field and current reversals. Quenching-in experiments, applied to vary the carrier density in a reversible way, have been performed by annealing the sample at a given temperature, T_A, for 30 minutes, followed by a rapid cooling in water to freeze-in the structural properties at T_A.

The Hall effect is positive for phosphorus-doped a-Si:H, a-SiC:H, and also for intrinsic a-Si:H, determined by photo-Hall experiments. For boron-doped a-Si:H, we detected a negative Hall voltage. Ignoring the anomaly and applying the standard transport equations, we calculate the Hall coefficient by:

$$R_H = (U_H/I)\,(d/B)\,f_{geo} \tag{17}$$

where I is the current, d is the specimen thickness, and f_{geo} is the Van der Pauw geometric factor (≈ 1). The Hall mobility, μ_H, is given by:

$$\mu_H = R_H\sigma \tag{18}$$

where σ = conductivity. The carrier density, n_H, is given by:

$$n_H = 1/(R_H q) \tag{19}$$

These equations are usually applied to doped semiconductors where one type of carrier is dominating the transport. Due to the dominance of electrons in intrinsic a-Si:H, we also apply these equations to interpret the photo-Hall data of i-a-Si:H.

Fig. 15 show measured conductivities, σ, Hall mobilities, μ_H, and the carrier densities, n_H, versus 1/T. The Hall mobilities are in the range $\mu_H < 0.1$ cm^2/Vs, and are decreasing with increasing doping concentration. While μ_H is approximately temperature independent, n_H is activated with energies 140-180 meV. In contrast, sweep-out data indicate that the band-tail carrier density, n_{BT}, is approximately temperature invariant. To clarify this contradiction, we have performed quenching-in experiments to utilize the fact that the value of n_{BT} is not uniquely defined by the
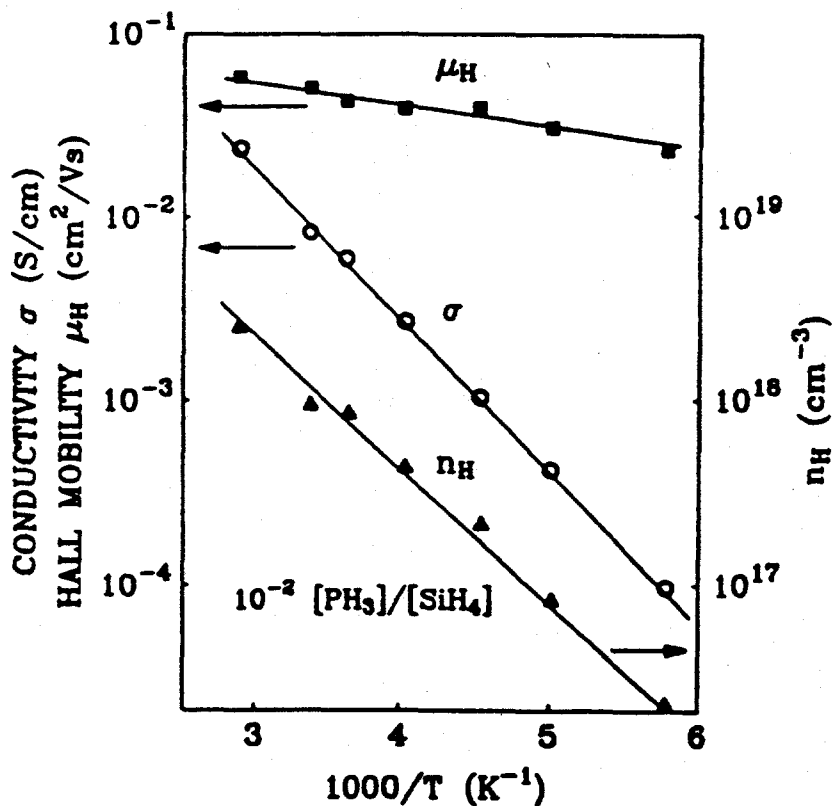

FIGURE 15. Hall mobility, H, conductivity, σ, and Hall carrier density, n_H, measured as a function of temperature.

doping level but depends on the thermal history of the sample. Above the equilibration temperature, the dopant and defect states come into equilibrium and have temperature dependent concentrations. Consequently, the equilibrium value of n_{BT} is also temperature dependent in this regime. The data to the right in Figs. 16 represent the initial state. We find that the carrier densities, n_H, deduced from Hall data are a constant factor larger than n_{BT}, measured by sweep-out experiments. μ_H and n_{BT} follow the same temperature dependence. μ_H is found to be independent of the carrier density in the thermal quenching experiments but smaller for a constant factor given by vH/n_{BT}, than μ_D. In general we find the basic relation:

$$n_{BT}\mu_D = n_H\mu_H \tag{20}$$

The interpretation of n_H is up to now not very well understood, whereas the band-tail carrier density, n_{BT}, has been investigated in detail. To calculate n_{BT} from Hall experiments we replace n_H in Eq. 19 by $n_H = n_{BT}\mu_D$. This gives the Hall coefficient relevant for a-Si:H and alloys,
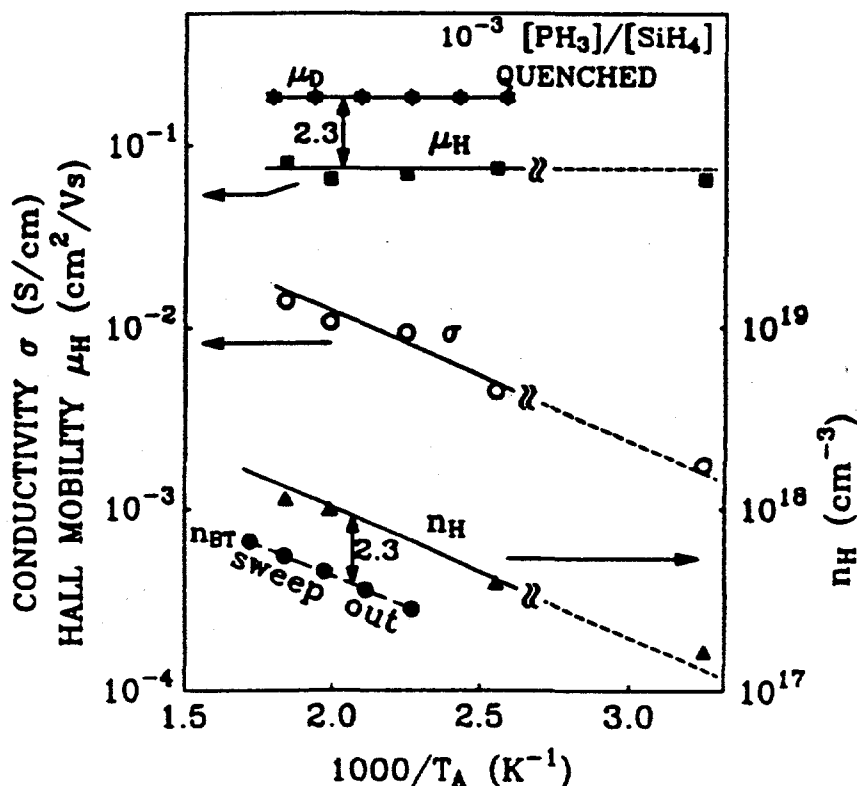

FIGURE 16. Variations of μ_D, μ_H, N_{BT}, σ and n_H as a function of annealing temperature.

$$R_H = 1/(n_{BT}q) \, \mu_H/\mu_D \tag{21}$$

We have measured Hall mobilities measured on a variety of differently doped a-Si:H layers. Highest mobilities of $\mu_H \simeq 0.1$ cm^2/Vs are deduced on intrinsic a-Si:H which are decreasing with doping. The Hall mobility of holes is lowest and in the range $(3\text{-}4) \times 10^{-2}$ cm^2/Vs. If we take the tail slope, E_0, as a measure of disorder, we can argue that n_H roughly scales as $1/E_0$, because an increase in disoreder is expected to reduce the free mobility. This would explain why the value for holes is about half that for electrons. The speculation that increasing lattice disorder, introduced by doping, is deteriorating μ_H is supported by measurements performed on silicon carbon alloys.

Fig. 17 shows data deduced on a-SiC:H. With increasing carbon content but constant phosphorus gas phase doping ratio of 10-3, μ_H is continuously decreasing with a significant drop for [CH$_4$]/[SiH$_4$+H$_4$+PH$_3$] > 50%. We assume that this is due to the increasing lattice disorder in the a-SiC:H alloy which leads to a significant broadening of the conduction band tail. A reasonable consequence is a shift of the
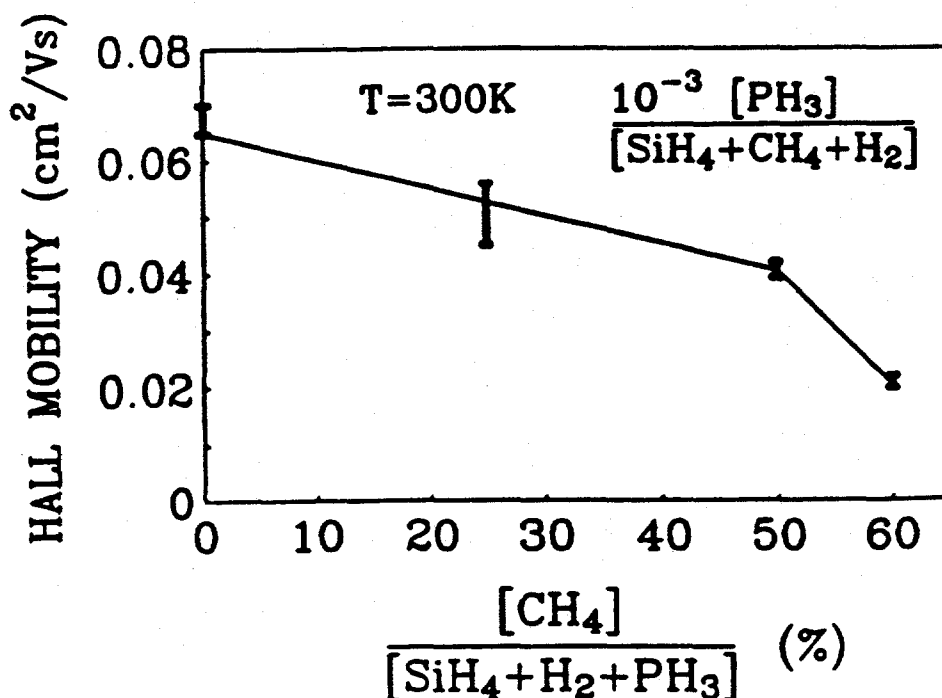

FIGURE 17. Hall mobility in a-Si:C, showing the decrease in μ_H as the carbon concentration is increased.

transport path deeper into the mobility gap where the wave function is more localized and carrier propagation perpendicular to the electric field therefore is slowed down. This speculation is supported by the fact that n_H is activated at higher doping levels. If the wavefunction overlap to neighboring sites is governing the Hall mobility, we also speculate that the smaller localization length of holes ($\simeq 5$ Å) compared to electrons ($\simeq 10$ Å) is also a reason for the much smaller Hall mobility of holes than of electrons.

2. Space charge limited currents at low temperature in a-Si:H

We have completed our studies of low temperature transport with measurements of transient and steady-state space charge limited currents (SCLC) performed on n+-i-n+ and p+-i-p+ structures in the low temperature regime T<100 K. Various junctions of thicknesses d_i = 2.5 and 3.5 µm (n+-i-n+) and d_i = 0.6, 1.1 and 2.0 µm (p+-i-p+) were prepared by conventional RF-glow-discharge
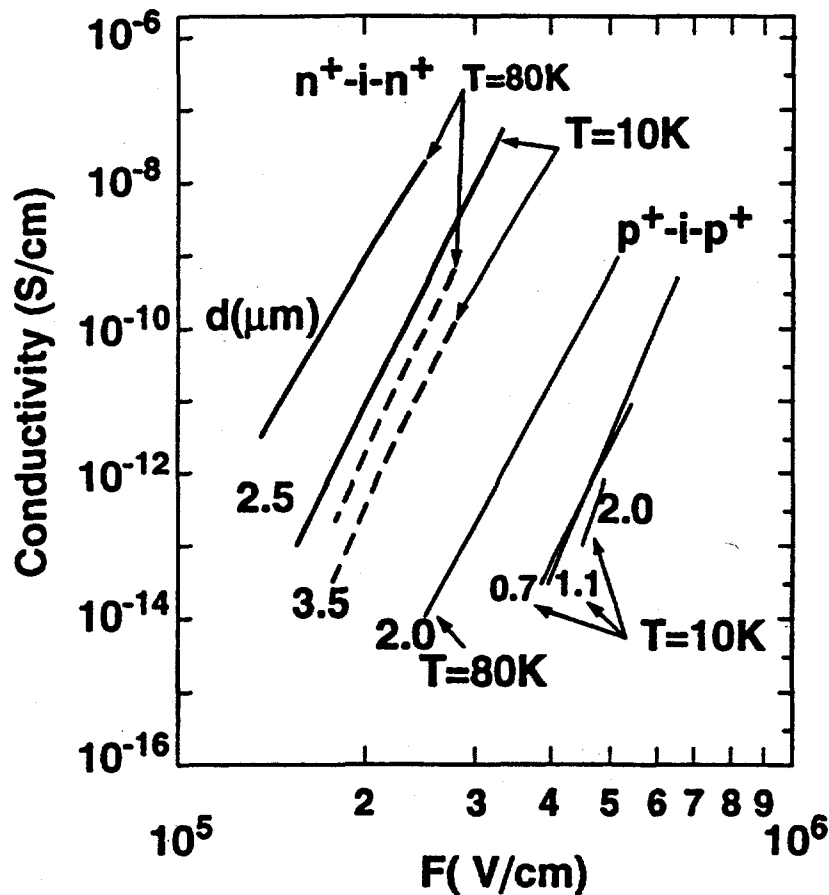

Fig 18. Space charge limited currents measured at T = 10 K and 80 K on n+-i-n+ (electrons) and p+-i-p+ (holes) junction.

deposition. Figure 18 summarizes conductivity data measured at T = 10 and 80 K, at fields above 10^5 V/cm. It is obvious that the conductivity enhancement takes place in the SCLC regime because data show the onset of the SCLC regime at about 10^3 V/cm. The conductivity increases rapidly with field and can be described by $\sigma \sim F^\gamma$ where $14 \le \gamma \le 17$. The thickness dependence is more pronounced in the n+-i-n+ than in the p+-i-p+ layers. Although the enhancement is related to space charge limited currents, the thickness dependence of the field enhancement at low temperatures (T = 10 K and 80 K) does not obey the usual scaling law. We attribute this to a combination of a field dependent variation of the transport level, the dominance of field over thermally induced carrier transitions, and band tail hopping as major carrier propagation mechanism. Considerably higher fields have to be applied in the case of hole transport (p+-i-p+) than in electron transport (n+-i-n+) in order to achieve comparable conductivities. A rise in temperature from 10K to 80K increases the conductivity, but the field enhancement is still overwhelming.

Transient SCLC currents measured at 80 K are shown in Figs. 19 (electrons) and 5 (holes). The current drops steeply after applying the electric field. The electron transients exhibit a change of slope, at a decreasing time with increasing field, after which the current decays slowly to the final dc level. We interpret this feature as
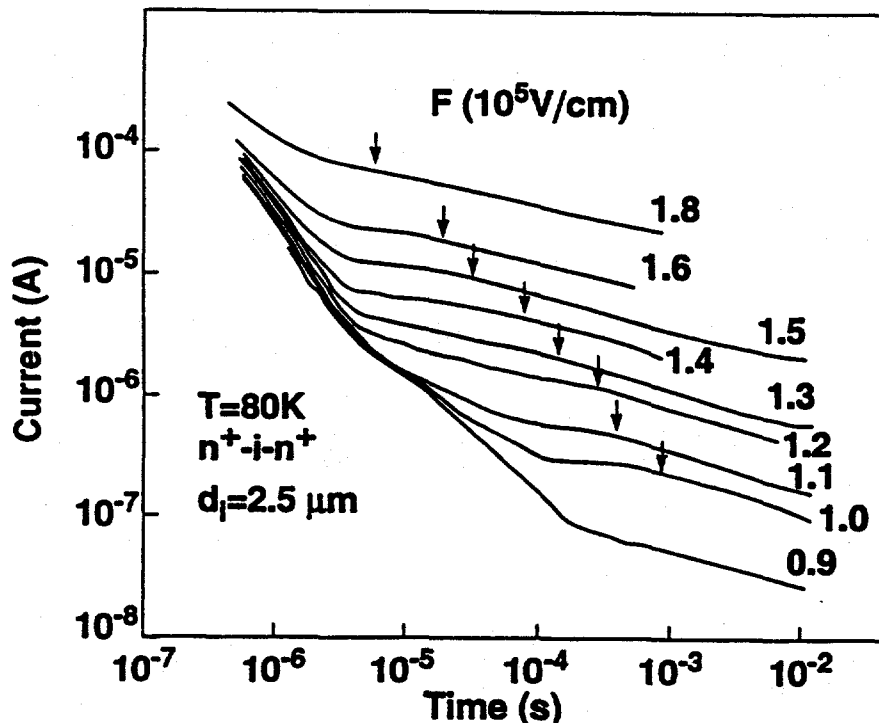

Fig 19. Electron transient space charge limited currents measured at T= 80 K on the 2.5 μm (a) and 3.5 μm (b) thick n+-i-n+ junctions. Arrows indicate the transit time.

indicating the transit time of carriers, as is expected in transient SCLC measurements. The feature is blurred by carriers dispersion, but is sufficient to evaluate in the electron drift mobility. We define the transit time t_T as the moment when the current decay turns into the shallow time dependence (see arrows in Fig. 19). Knowing t_T enables the determination of an approximate carrier mobility given by:

$$\mu (F) \simeq \frac{0.78 \ d_i}{F \ t_T} \qquad (23)$$

where d_i is the thickness of the intrinsic layer and F the applied field. In the dispersive transport regime with carrier interactions dominated by an exponential trap distribution, the transit time is,

$$t_T = t_T^* \ (0.78)^{1/a} \qquad (24)$$

where t_T^* is the space charge free transit time and $\alpha = kT/kT_o$ where kT_o is the characteristic energy of the exponentially distributed band tail.

The deduced drift mobilities are displayed in Fig. 20 and show a strong field dependence. For comparison we also plot data measured by time-of -flight experiments at 80 K on p-i-n junctions in the space charge free regime. The data show that the field dependent increase of μ in intrinsic a-Si:H, determined by SCLC experiments can be described approximately by an exponential law, F^Y. The SCLC data also show a stronger field dependence than the data derived from TOF experiments which indicates that the SCLC transport takes place deeper in the tail. The mobility depends on thickness, consistent with the dispersive nature of field induced transport. However, there is some discrepency between the SCLC and TOF measurements of mobility which may originate from the different carrier generation mechanisms.

3. Calculation of SCLC with a field dependent mobility

There is a striking similarity of field enhanced characteristics, whether measured on intrinsic a-Si:H with space charge limitations or on doped a-Si:H in the SCLC free case. The explanation is that the SCLC properties are modified by the large enhance the carrier mobility. We show this by solving the Poisson equation for a semiconductor with no traps but a strong field dependent mobility given by,
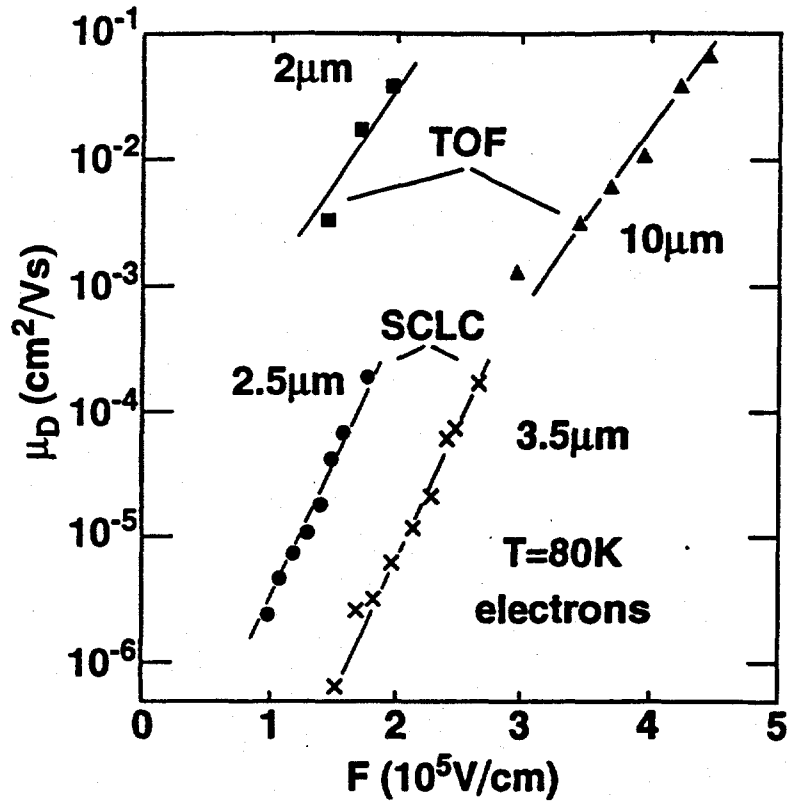
Fig 20. Electron drift mobilities deduced at t = 80 K by transient space charge limited currents on n+-i-n+-junctions of thickness 2.5 and 3.5 µm and by time-of-flight experiments on p-i-n junctions of 2 and 10 µm thickness.

$$\mu(F) \simeq \mu_o \, F^\gamma \qquad\qquad (23)$$

where the data find $10 \leq \gamma \leq 17$. The power law enables a simple analytic approach and has been derived from data on doped a-Si:H where the band tail carrier density is invariant and the increase in σ is proportional to the increase in μ. Poisson's equation is solved for the condition that the conductivity, $\sigma = nq\mu$, is constant. The strong field dependent mobility modifies the carrier concentration and prevents the build up of an inhomogeneous field, given by,

$$F(x) \sim x^{(1/(\gamma + 2))} \qquad\qquad (24)$$

For large values of γ, F is weakly varying and there is also a moderately inhomogeneous distribution of carriers between the contacts given by,

$$n(x) \sim x^{-(\gamma + 1)/(\gamma + 2)} \qquad\qquad (25)$$

31

To achieve this mobility dominated SCLC, the quasi Fermi-level has to shift into the band tail region where the density of state is rapidly increasing. The further enhancement in conductivity is then dominated by field stimulated band tail hopping, a phenomenon which is inherently related to band tails and therefore should be a universal feature of amorphous semiconductors.

Thus the evaluation of $\sigma(F)$ and $\mu(F)$ indicate that the low field enhancement of σ is driven by carrier injection, but dominated by the strong enhancement in carrier mobility towards higher fields. The tail regions of a-Si:H change from insulating to highly conductive in the presence of high fields. This is due to the field alignment of accessible states and comparable with the field effect in resonant tunneling experiments on superlattices. A simple model demonstrates that the inhomogeneous carrier and field distribution typical of the SCLC regime is supressed by the field dependent mobility. So far, field dependent transport has not been included in solar cell modelling and further studies are needed to determine whether this is a significant mechanisms at the relevent fields and temperatures of cells.

D. HYDROGEN STRUCTURE AND DIFFUSION

The intermediate scale structure, the growth process at the film surface, and metastability are all intimately related to hydrogen bonding and transport in a-Si:H. We are investigating several aspects of hydrogen transport and models for hydrogen bonding in amorphous silicon.

1 Hydrogen Diffusion in H-depleted material

We have measured H diffusion in hydrogen depleted samples to study the effects of the hydrogen concentrations on the diffusion porocess. Concentration profiles for D diffusion through H-depleted a-Si:H are presented in Fig. 21(a). For high concentrations the profiles exhibit the standard complementary error function (erfc) profiles which arise from Fickian diffusion with a concentration independent diffusion coefficient from a half plane assuming a constant concentration at the surface. For low concentrations, the profiles deviate from an erfc form and become exponential. Such a behavior is characteristic of trap dominated diffusion where the total concentration is less than the trap concentration. The concentration where the profile departs from an erfc profile is an accurate measure of the trap concentration.

32

From Fig. 21(a), the trap density is estimated to be about $8\text{-}9\text{X}10^{19}$ cm^3. This interpretation of the profiles is supported by the attenuated D diffusion profiles which consist nearly entirely of exponential decays. The transition from erfc to exponential occurs at the same concentration and the exponential slopes are the same. The exponential slopes are virtually the same as the SIMS resolution so the actual slope is probably much steeper. Hence, one cannot deduce a capture radius for these traps.

Interestingly, diffusion into normal a-Si:H containing 10 at.% H also presents an trap dominated diffusion profile as shown in Fig. 21(b). The high concentration profile is erfc becoming exponential at smaller concentrations. The trap density estimated from this profile is about $1\text{X}10^{21}$ cm^{-3}. Because of the high trap density,
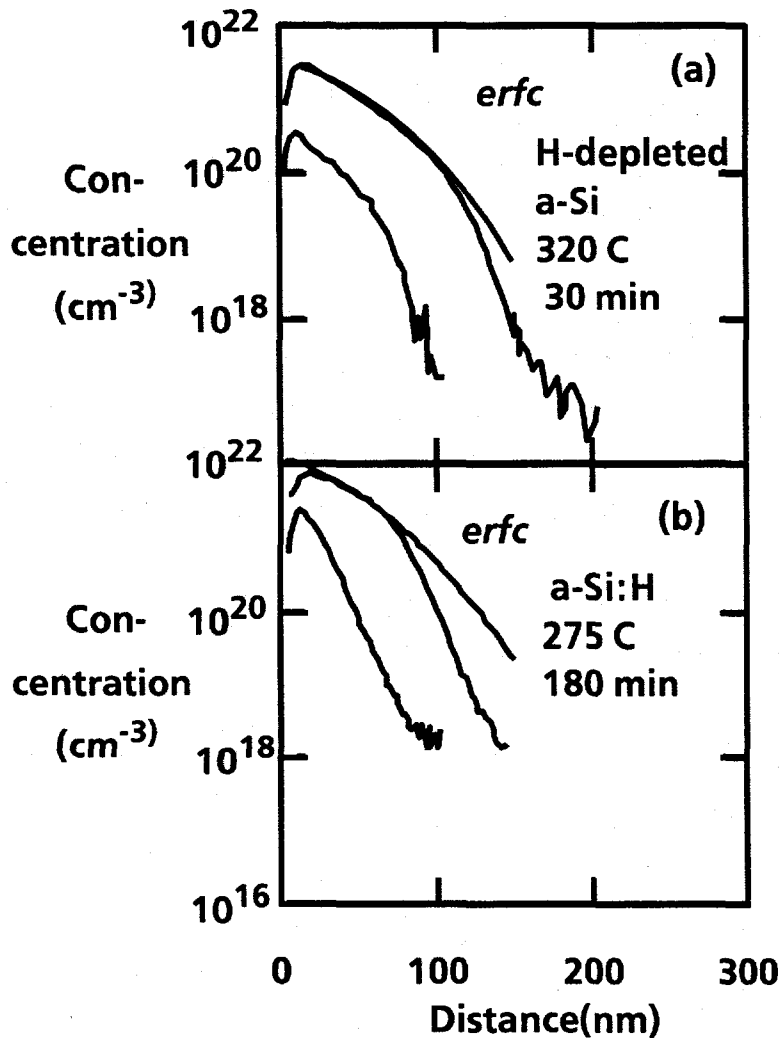

Fig. 21 (a) and (b) The deuterium concentration versus distance for exposure to a deuterium plasma and a plasma attenuated by a stainless steel mesh at indicated temperatures and times. (a) H-depleted a-Si:H. (b) as-deposited a-Si:H subjected to plasma at a temperature of 275C, for 3 hrs. The top solid line indicates an erfc profile.
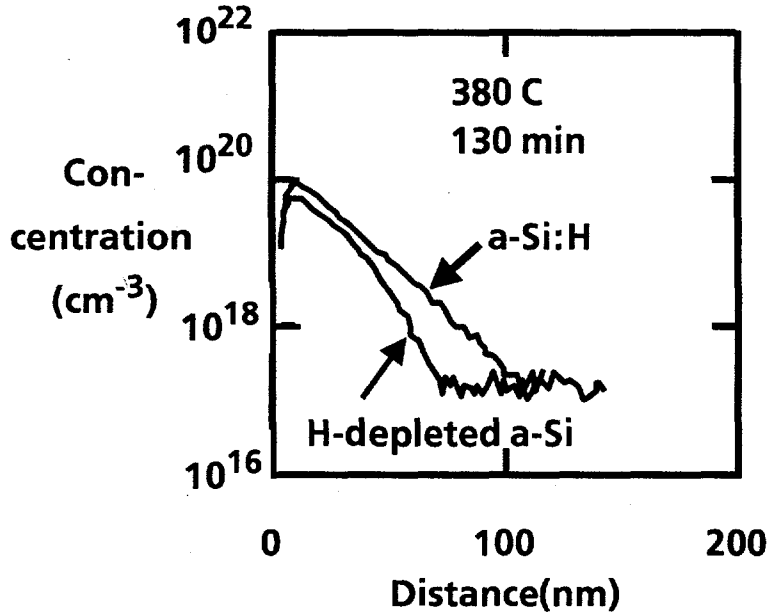
Fig. 21(c) Deuterium profiles after exposure to an attenuated deuterium plasma for both a-Si:H and H-depleted a-Si. The substrate temperature for deposition of the a-Si:H was 380C.

the attenuated D profile is nearly completely exponential. The low H content film with 3 orders of magnitude higher spin densities than normal a-Si:H have trap densities for H diffusion that are about one order of magnitude lower. Clearly, the traps cannot be dangling bonds in both cases. An additional important point is that the exponential slope in the normal a-Si:H is also broader despite having a higher trap density. This is especially apparent in Fig. 21(c). An H-depleted sample and an as-deposited sample were simultaneously exposed to an attenuated remote D plasma. The trap density is higher in the normal a-Si:H, however, leading to the pure exponential decay rather than a more rounded profile for the H-depleted sample. The H-depleted sample has a smaller trap density but the traps are more effective capturing the D. This requires that traps in the normal a-Si:H must have either a smaller cross section, or there is re-emission from the traps during diffusion. The latter possibility is equivalent to positing that the traps are shallower in normal a-Si:H compared to the H-depleted Si.

The effect of time on diffusion in H-depleted a-Si:H is shown in Fig. 22. Consistent with the interpretation that the exponential portion is due to trapping of the mobile D, neither the exponential slope nor the concentration at which the trapping behavior dominates differs appreciably as time increases. Note that the trap concentration is nearly exactly equal to the hydrogen concentration of the film--a result further investigated below. The diffusion coefficient derived from the
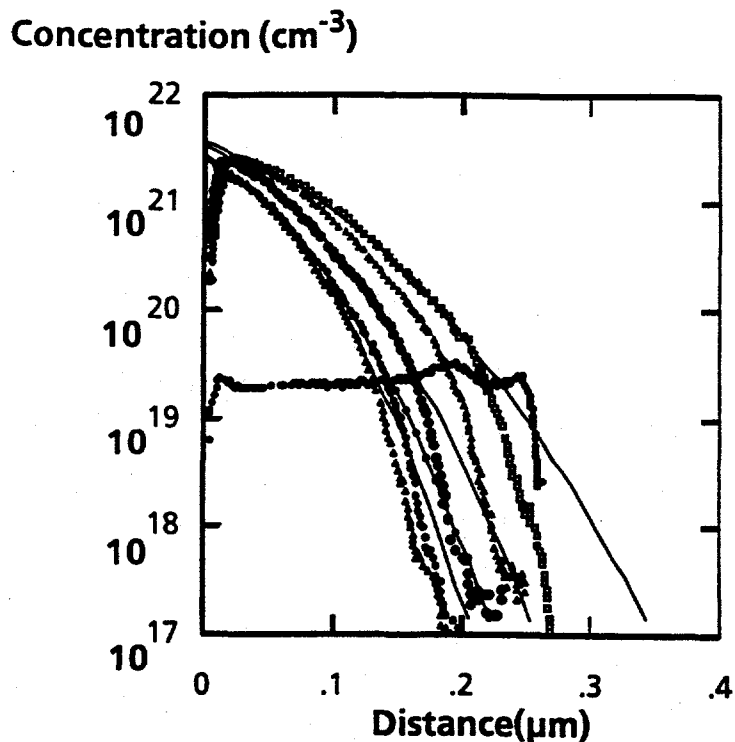
34

Concentration (cm⁻³)

Fig. 22   Effect of time on D diffusion profiles. D concentration versus distance for various time for H-depleted a-Si.   The H concentration for the first curve is also indicated. The solid line represents the best fit erfc to the data. The concentration where the data deviates from an erfc profile indicates the trap density which does not appear to change with time.

data in Fig. 22 shows a weak time dependence given by a power law dependence characteristic of dispersive transport. From such time dependence we can conclude that the distribution of mobile H is changing with time either due to redistribution within existing states or slow structural changes occurring on time scales comparable to or longer than the diffusion times.

2. Comparison of inter-layer and external hydrogen diffusion

A comparison of diffusion between layers and diffusion from a plasma are shown in Fig. 23 for normal a-Si:H. Layer diffusion is significantly reduced compared to diffusion from a plasma, consistent with the reduced diffusion for low hydrogen concentration. Note that the exponential slope region for layer diffusion has the same slope as for diffusion from a plasma as expected for diffusion in the presence of traps. Measuring the diffusion as a function of temperature indicates that the activation energy for layer diffusion is about 1.2-1.3 eV while the activation energy of diffusion from a plasma depends on the concentration but is only about 0.5 eV
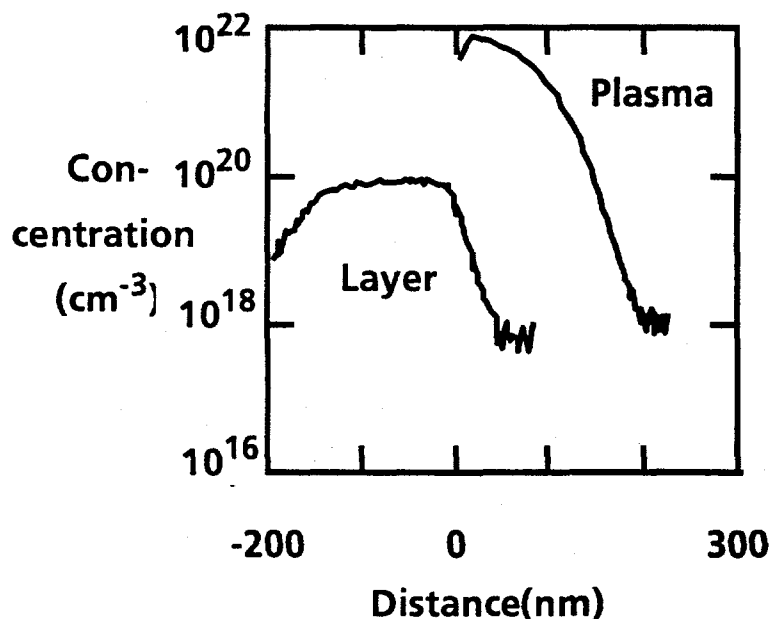
Fig. 23   Comparison of layer diffusion and diffusion from a plasma for a-Si:H.

This difference in diffusion can readily be explained by diffusion in the presence of traps.

The unexpected increase in trap density with H concentration is further investigated in Fig. 24. H-depleted a-Si was exposed to different concentrations of H plasma to change the H concentration without altering the Si network structure due

Fig. 24   Effect of H concentration on the diffusion of D in H-depleted a-Si. The H was introduced by 2.5 hrs, 430 C remote plasma exposure at various attenuations. The H concentration profiles are also shown along with the estimated trap concentrations and a least squares erfc.

Fig. 25 Effect of extended annealing on the D diffusion profiles for two different samples a-Si:H samples with slightly different H con-centrations. The annealing times at 350C in hours preceding deuteration are indicated.

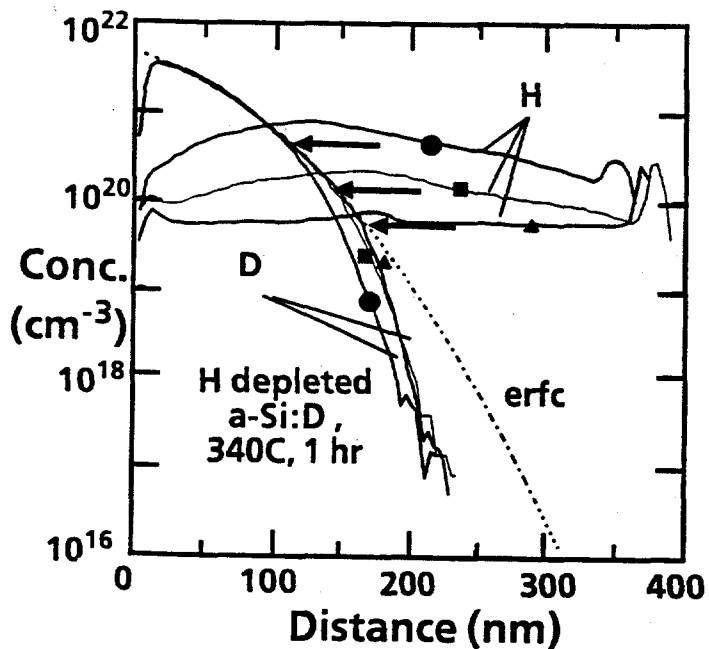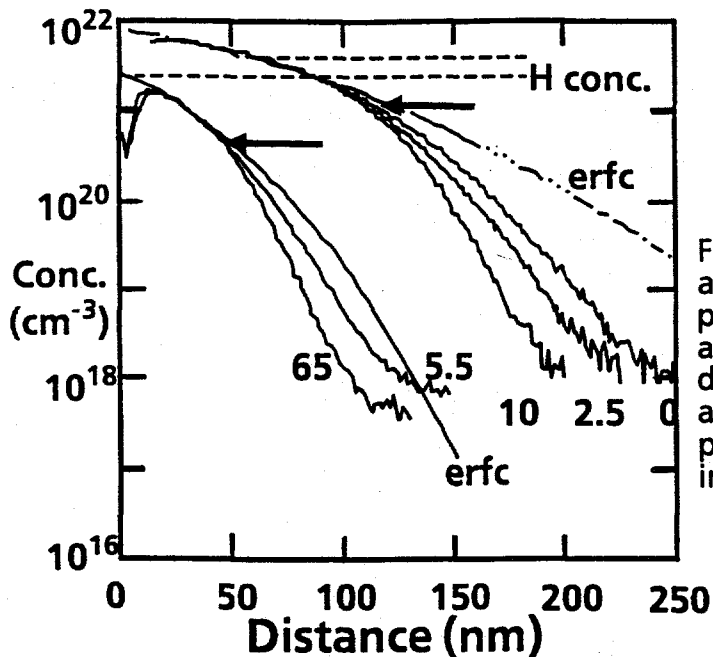to changes in film growth conditions. The corresponding trap levels derived from the point of deviation from an erfc profile are indicated by the arrows along with the corresponding H concentrations. This data further confirms the general trend noted earlier that increasing the H concentration actually increases the number of traps. The small curvature of the profiles for concentrations below the trap levels are indicative of comparatively shallow trap levels not much deeper than the level controlling diffusion in the high concentration limit. Clearly, these traps cannot be dangling bonds and are apparently associated with H since their concentration increases with H concentration.

As a result of these experiments as well as experiments showing that H forms platelets in c-Si, we annealed normal a-Si:H samples for extended periods of time to see if we could alter the trapping characteristics by causing local redistributions in H bonding. Slow changes in the trapping characteristics were readily apparent as shown in Fig. 25. Annealing increases the slope of the exponential distribution but did not alter the number of traps. Such behavior is characteristic of traps becoming deeper rather than more numerous. Depletion of H near the surface arising from the extended annealing would result in an increased the trap density. This behavior is also not expected of dangling bond traps.

In an effort to identify possible origins of traps, we compare deuteration profiles for three markedly different Si networks: low temperature H platelet nucleated c-Si, poly crystalline Si, and H-depleted Si (Fig. 26). Since the diffusion coefficients are highly concentration dependent, nearly equal surface concentrations were selected. From the similar slope of the curves close to the surface in the high concentration region, it is apparent that the diffusion coefficients are similar. Thus, the high concentration diffusion appears to be rather independent of the changes in the silicon network. The small convex portion observed in both the c-Si and the poly-Si is characteristic of concentration dependent trapping. Deviations from the erfc profile occur for concentrations around the mid-10^{19} cm^{-3} level indicating that the number of traps is roughly the same. Below this level, however, the profiles differ significantly. The H-depleted Si profiles are much sharper than the poly-Si and platelet c-Si indicative of either higher cross sections and/or deeper traps. This remarkable finding that the effect high concentration diffusion does not depend significantly on the form of the Si network will be discussed further below.
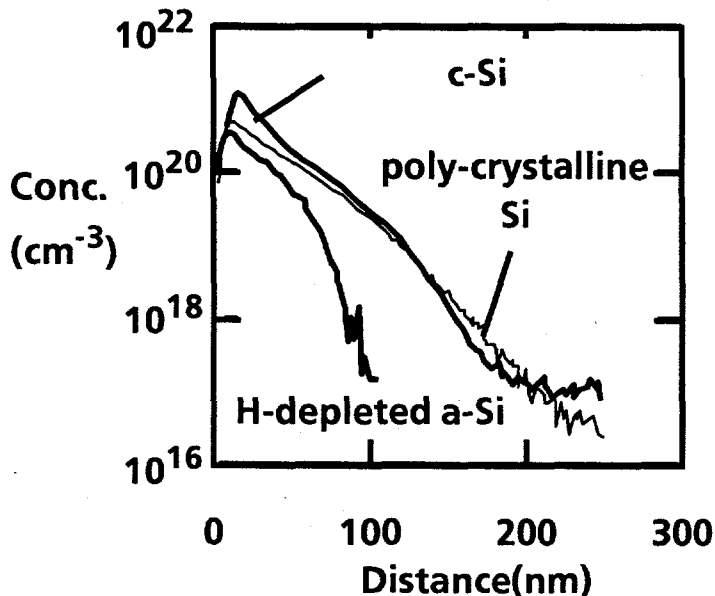
Fig. 26. Comparison of D diffusion in H-depleted Si, polycrystalline Si, and c-Si containing H platelet nucleation sites. The c-Si sample was n-type Si, (100), float zone with a [P] =8X1017 cm-3 exposed to a D plasma at 150C, 20 min then at 275C, 60 min. The poly crystalline Si sample consisted of fine grained poly-Si undoped and deuterated at 250C 30 min/, The H-depleted a-Si was deuterated in an attenuated deuterium plasma at 320 C for 30min.

38

3. LDA calculations of Si-H bonds

We have carried out a large number of calculations for various configurations of H in its interactions with Si. The first-principles calculations of Si-H structures are based on density-functional theory (in the local-density approximation) and ab initio pseudopotentials. Spin polarization is included where necessary. The accuracy of the calculated energy values depends on the configuration under study, but as a rough guideline an uncertainty of 0.1 eV can be assumed.

Figure 27 displays an energy scale showing the energy per H atom associated with a number of these configurations. The zero of energy is chosen here to correspond to the energy of a neutral H atom in free space. Our calculated energy for H in an H_2 molecule is -2.31 eV (per atom); this implies a binding energy for the H_2 molecule of 4.62 eV, which is very close to the experimental value 4.52 eV. Referred to bulk Si and free H atoms we find the energy of SiH_4 to be -2.22 eV (per H atom). Note that
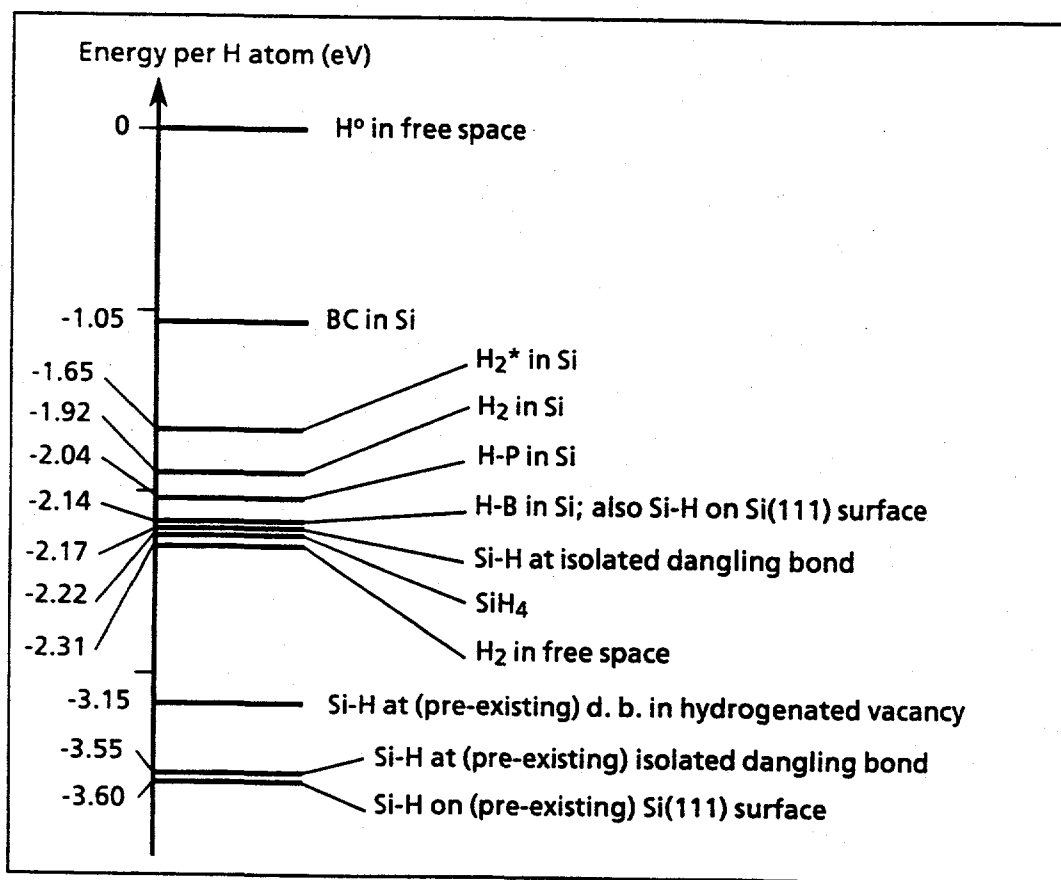
Fig. 27. First-principles energies for various configurations of H in silicon. The zero of energy corresponds to a free H atom.

39

this value places SiH_4 at an energy 0.09 eV (per H atom) above the H_2 molecule; this translates into a heat of formation for SiH4 (expressed with respect to Si bulk and H_2 molecules) of 0.36 eV, which is (fortuitously) exactly the same as the experimental value. The value for "BC in Si" refers to the lowest energy configuration for an isolated neutral H interstitial in crystalline Si, which is at the bond-center site. Its energy is 1.05 eV below the value for H in free space.

For the H_2 molecules in the Si crystal we find that the molecule is most stable at a tetrahedral interstitial site, oriented along [100].The energy of this configuration is -1.92 eV per H atom. This implies that when two isolated interstitial H atoms (at BC) combine and form an H_2 molecule in Si, an energy of (-1.05) - (-1.92) = 0.87 eV per atom is gained (or 1.74 eV per molecule). We find the energy of this configuration to be -2.14 eV. This shows that the energy of H on the Si(111) surface (i.e. tying off a dangling bond) is only slightly smaller than its energy in an SiH_4 molecule.

In the case of the Si-H bond on the Si surface, the formation energy is not the only energy value which is relevant to characterize the configuration. Instead of comparing the energy with respect to Si bulk, we can ask how much energy is involved in removing the H atom from the surface, leaving a dangling bond on the bare surface behind. Detailed investigations of this surface have been previously performed with first-principles techniques; it was found that the energy of the relaxed 1x1 surface is 1.46 eV (per atom) higher than the bulk. We therefore conclude that when we remove a H atom from the hydrogenated (111) surface, leaving a dangling bond behind (and neglecting any interaction between this dangling bond and neighboring H atoms), the energy cost would be

$$2.14 + 1.46\,eV = 3.60\,eV. \qquad (26)$$

This value is also included in the diagram of Fig. 27.

Figure 27 shows that the formation energy of an Si-H bond on the (111) surface is -2.10 eV. As discussed above, this energy value includes the energy necessary to create the surface; i.e., starting from bulk Si and H atoms, one would gain 2.1 eV per H atom if the bulk crystal would separate, creating two surfaces, and H would tie off all the resulting dangling bonds. Kinetic barriers to this process may of course exist; but it is suggestive that this energy of -2.1 eV is lower than that of the H_2 molecule in Si (-1.92 eV), and much lower than that of the isolated interstitial (-1.05 eV). This low

value is a consequence of the high strength of the Si-H bond, and indicates that, rather than simply sit in solution, H will attempt to disrupt the bulk crystal structure and form Si-H bonds. This mechanism is the likely driving force behind the formation of H-induced platelets; although the microscopic structure of these extended defects is still being debated, it is well established that they contain H bonded in Si-H bonds.

4. Model for H Trapping in a-Si:H

Diffusion in the presence of traps is modelled by the distribution shown in Fig. 28.

E_m Transport level

E_s ── ── ── ── Shallow
── ── ── Traps

── · ── · ── · ── · ── μ_H

── ── H related   Deep
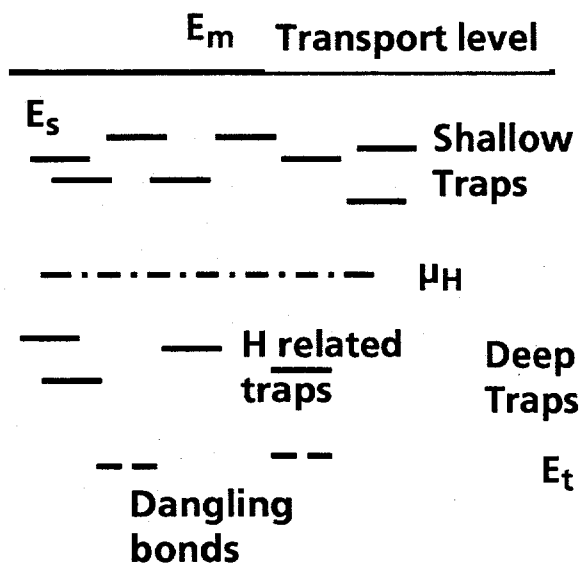── traps   Traps

── ── E_t
Dangling
bonds

Fig. 28   A hydrogen trap model accounting for experimental results. The transport sites at the transport energy have an energy E_m, while the shallow traps which release in a time short compared to the experiments are at energy E_s. The deep states (energy E_t) are in general separated from the shallow states. In H-depleted a-Si, the dangling bond states are significantly deeper than the shallower states occurring in normal a-Si:H which scale with H concentration. The hydrogen chemical potential, μ_H separates the occupied sites from the unoccupied ones and resides in an approximate minimum of the density of trapping sites.

In this model, the H binding (or trapping sites) are divided roughly into three types of states: mobile transport states, shallow traps, and deep traps. These states are more or less separated in energy and these is a minimum in the density of states between the shallow and transport states and the deep traps. The approximate energies and concentrations of these three types of states are E_m, E_s, and E_t and N_m, N_s, and N_t, respectively. The hydrogen chemical potential generally resides between E_s and E_t or below. In such a model, the effective diffusion for H in the shallow traps is given by $D_{eff,s} = D_0(N_m/N_s)\exp[-(E_m-E_s)/kT]$ where D_0 is the microscopic diffusion coefficient in the transport states. The trapping and diffusion of H is then given by

41

$$\frac{\partial H_s}{\partial t} = D_{s,eff} \frac{\partial^2 H_s}{\partial x^2} - \frac{\partial H_t}{\partial t} \qquad (27)$$

$$\frac{\partial H_t}{\partial t} = 4\pi R_c D_{s,eff} H_s N_t^{free} - v H_t \qquad (28)$$

where $v = 4\pi R_c D_{s,eff} N_s \exp[-(E_m-E_t)/kT]$, N_{tfree} is the number of unoccupied traps and R_c is the capture radius. A similar pair of equations hold for deuterium with D_t and D_s replacing H_t and H_s, respectively. Since H and D compete for the same traps $N_{freet} = N_t - H_t - D_t$ where D_t is the trapped deuterium. For a spatial region and times where the shallow and deep traps have equilibrated, the left hand side of the trapping equation may be set equal to zero and the result substituted into the diffusion equation, yielding a diffusion equation for the total concentration with an effective diffusion of $D_{eff} = D_{eff,s} (N_s/N_t)\exp[-(E_s-\mu_H)/kT]$ assuming that μ_H is above E_t.

For regions of the material where $\partial H_s/\partial t$ is small, the profiles exhibit an exponential distribution of the form $H(x) = H_0\exp(-x/x_0)$ where the slope x_0 is approximately given by

$$x_0 = [4\pi R_c (N_t^{free} - N_t^{free,equil})]^{-\frac{1}{2}} \qquad (29)$$

where $N_{tfree,equil}$ is the equilibrium free trap density. Because N_{tfree} approaches $N_{tfree,equil}$ as E_t approaches E_s, the slope is broader for shallower traps than for deeper ones (Fig. 29). The capture radii of traps is not expected to vary widely since trapping is not likely to be dominated by capture of charged H by traps of the opposite charge. Thus, a change in exponential slope without a corresponding change in the number of traps occurs because of changes in the depth of the traps controlling diffusion.

The expected behavior of diffusion in the model can be readily determined by solving Eq. (27) and (28) numerically assuming a constant shallow concentration at the surface. The resulting numerical solutions verify the conclusions reached above and can also accurately reproduce the data.

Considering the data, we conclude that the trap density in the as-deposited a-Si:H is $1\text{-}2 \times 10^{21}$ cm^{-3} while the trap density in the H-depleted a-Si is $8\text{-}9 \times 10^{19}$ cm^{-3}.

log C

erfc

N_t
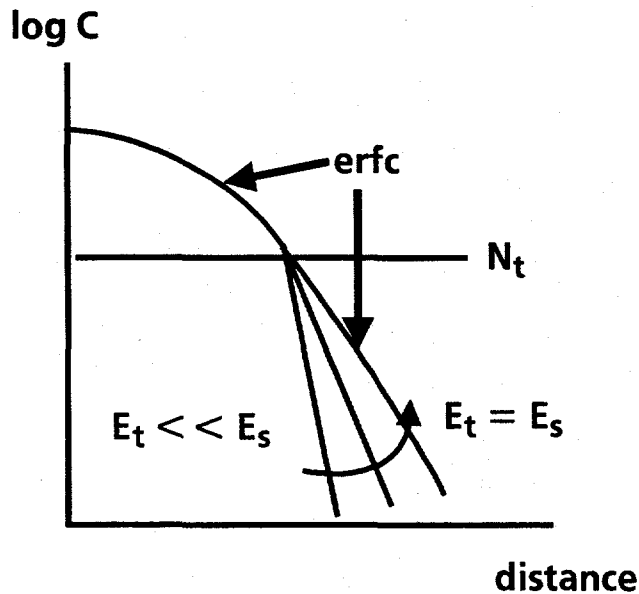
$E_t \ll E_s$ $E_t = E_s$

distance

Fig. 29 The effect of decreasing the trap energy until it merges with the shallow traps.

From the slope of the data, we estimate that emission from the traps in the as-deposited material is at least 64 times larger than for H-depleted material. This is a lower bound since the slope in the H-depleted material is SIMS resolution limited. Thus, we estimate that traps in H-depleted material is at least 0.2 eV deeper than the traps in as-deposited material and could be significantly more.

The changes in diffusion with concentration are also consistent with the trap model. If D is introduced from the plasma increasing the concentration, the chemical potential rises from near the trap level to close to the shallow level. The diffusion activation energy changes from near E_t to near E_s. We conclude that the chemical potential normally resides near the trap level 1.2-1.4 eV below the transport energy during layer diffusion. During deuteration from the plasma, the chemical potential rises to as high as 0.5 eV below the transport level. The lines shown in Fig. 29, are obtained by numerical solutions to Eqs. (28) and (29) with $E_t = 1.2$ eV and $E_s = 0.5$ eV below E_m and a shallow surface concentration of 1.5×10^{18} cm^{-3}. At temperatures where the layer and plasma diffusion merge, the thermally induced shallow D concentration becomes comparable to the concentration introduced from the plasma. Summarizing, to first order, most of the diffusion a-Si can be accounted for by a simple model of diffusion in the presence of

a fixed concentration of traps, the characteristics of which change with H concentration.

5. Hydrogen migration and electronic carriers in a-Si:H

To further investigate the connection between metastability and hydrogen, we have studied the interaction between electronic carriers and hydrogen diffusion by measuring the effects of an electric field on the migration. A representative SIMS deuterium depth profile from an unannealed diode is illustrated in Fig. 30 (dot-dashed line). The steepness of the composition profile at the interfaces of the deuterated layer is determined by the depth resolution of the SIMS experiments measurement, defined as the minimum depth x_s to achieve concentration decay by a factor of $1/e$. The resolution decreases with depth and increases from x_s ~8 nm at the outer (left-hand) edge of the a-Si:H:D layer to x_s ~11 nm at the right inner (right-hand) edge.
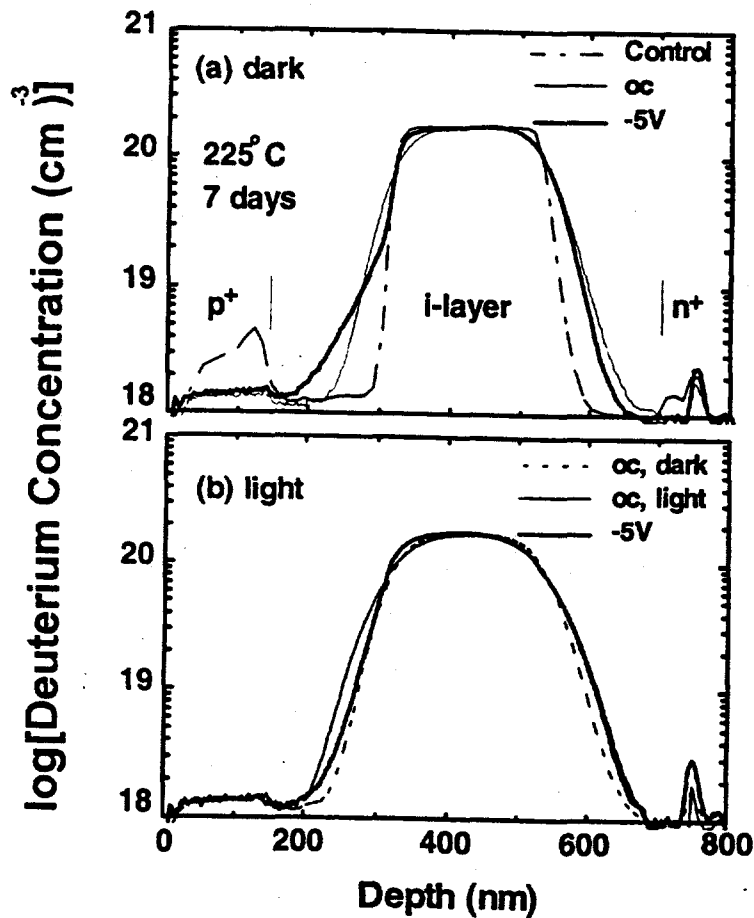

Fig 30. (a) Deuterium profiles for diffusion in the intrinsic layer of a p-i-n diode under open circuit (oc) and reverse bias. (b) corresponding profiles under illumination.

The additional depth profiles in Fig. 31 were recorded after annealing at 225°C for seven days under different bias and illumination conditions. The thin line in Fig. 31(a) shows the deuterium concentration in a control sample annealed under open circuit (oc) conditions, where diffusion takes place in only the small built-in electric field. Annealing in this case leads to a symmetrical broadening of the composition profile at the interfaces due to deuterium diffusion. The thick line in Fig. 31(a) is the corresponding profile after annealing under an applied reverse bias of 5 V, which yielded an average electric field E - 9.2×10^4 V/cm in the intrinsic layer. The diffusion profile is asymmetric in this case. At the right-hand side of the a-Si:H:D layer, deuterium diffusion into the bottom a-Si:H layer is only slightly less than under open-circuit conditions [thin line in Fig. 31(a)]. At the left-hand side, on the other hand, deuterium diffusion is strongly suppressed at the immediate vicinity of the edge (i.e., for concentrations above 2×10^{19} cm^{-3}). The deuterium profile in this case is almost indistinguishable from that of an unannealed sample (dashed-dotted line) and is determined by the SIMS depth resolution. The sharpening of the profiles under reverse bias is attributed to the suppression of hydrogen migration when electronic carriers are extracted from the diffusion region by the application of a reverse field.

The second effect arising from the application of a reverse bias is the appearance of a tail of deuterium atoms away from the left-hand edge of the deuterated layer (i.e., for deuterium concentrations below 2×10^{19} cm^{-3}) and extending the p+ layer. As will be discussed in more detail later, some samples also show a diffusion tail at the right hand side of the deuterated layer. The tails penetrate further into the a-Si:H layer than for diffusion under short-circuit conditions, which indicates enhanced deuterium migration. Note that due to the logarithmic scale, the number of deuterium atoms forming the tails is only a small fraction of the number of atoms diffusing under the same conditions under open circuit. In addition, the deuterium concentration decays approximately exponentially with distance, in contrast to the complementary error function (erfc)-like profile characteristic of diffusive motion.

The diffusion profiles for annealing under open-circuit conditions fit a complementary error function erfc [$x/2\sqrt{D_{eff}t_d}$)] where x is the depth in the layer and D_{eff} and t_d are, respectively, the effective diffusion coefficient and the diffusion time. This also applies for deuterium diffusion in to the bottom a-Si:H layer of a-si:H under reverse bias. The effective diffusion coefficient D_{eff} includes both the effects

45

of deuterium diffusion in a transport path consisting of interstitial sites and/or bond center sites, and capture and release by trapping sites. In the fitting procedure, the erfc were convoluted with the exponential function $S(x) = x_s^{-1} \exp(x/x_s)$ to account for the depth resolution of the SIMS analysis. The convolution is necessary to obtain reliable results for the diffusion coefficient when the deuterium penetration depth is not substantially larger than x_s. Displayed in Fig. 31 is the effective diffusion coefficient obtained from the fits to the profiles at the left-hand side of the deuterated layer for annealing under different conditions. The squares and dots correspond to values for the diffusion coefficient obtained for annealing at 225°C and 250°C, respectively.
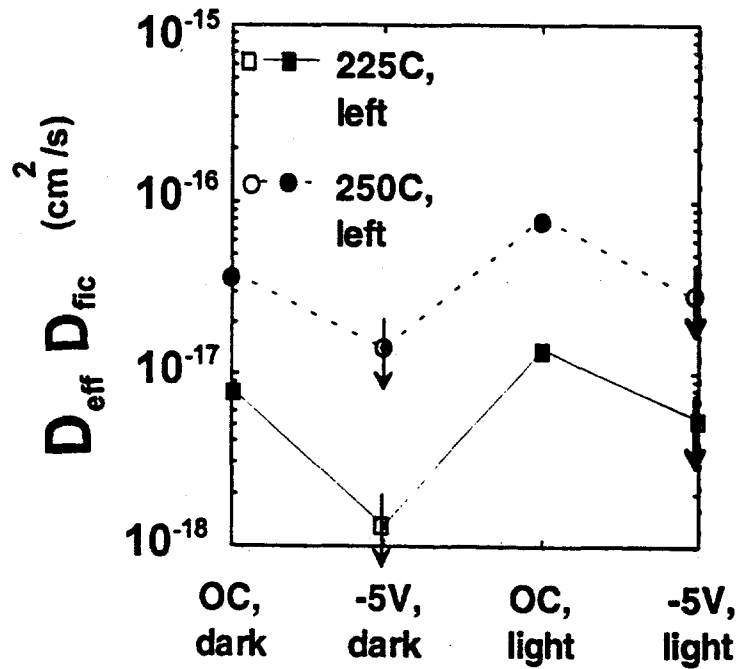

Fig 31. Effective and fictive diffusion coefficients for hydrogen diffusion under open circuit and under different bias and illumination conditions.

For annealing under reverse bias, the profiles differ appreciably from erfc and are affected by the SIMS depth resolution. As will be discussed in detail in Sec. IV, the shape of the profiles at the edge of the deuterated layer in this case is not associated with the effective diffusion coefficient. Fitting the profiles for high deuterium concentrations ($> 2 \times 10^{19}$ cm^{-3}) to an erfc yields, nevertheless, a fictive diffusion coefficient D_{fic} that describes the migration of the majority of deuterium atoms for short diffusion times. The upper limit for this fictive diffusion coefficient is indicated by the arrows superposed on the open symbols in Fig. 31. As mentioned previously,

migration is strongly suppressed in this case. Illumination during the thermal treatment enhances deuterium diffusion, but no enhancement is observed if the carriers are extracted from the diffusion region by the application of a reverse bias.

The dependence of the deuterium diffusion coefficient on illumination and bias illustrated in Fig. 32 clearly demonstrates that hydrogen motion in undoped a-Si:H is controlled by the concentration of electronic carriers in the diffusion region. In order to further study the interaction between hydrogen migration and carrier concentration, we measured the dependence of the deuterium concentration profiles on the reverse field applied to the diodes. Fig. 32 compares diffusion profiles on samples annealed for seven days at 225°C under different reverse biases. The dashed and solid lines are corresponding profiles for an unannealed sample and for a sample annealed under open-cirduit conditions. Most of the bias-induced changes in the profiles occur for relatively small reverse bias (less than 2 V, corresponding to electric fields of 2×10^4 to 4×10^4 V/cm in the intrinsic region). In this bias range, the profiles sharpen at the interface with the deuterated layers and the exponential tail of fast-migrating atoms forms. It is interesting to note that the profiles in the tail region do not change for reverse biases exceeding 2 V, and no
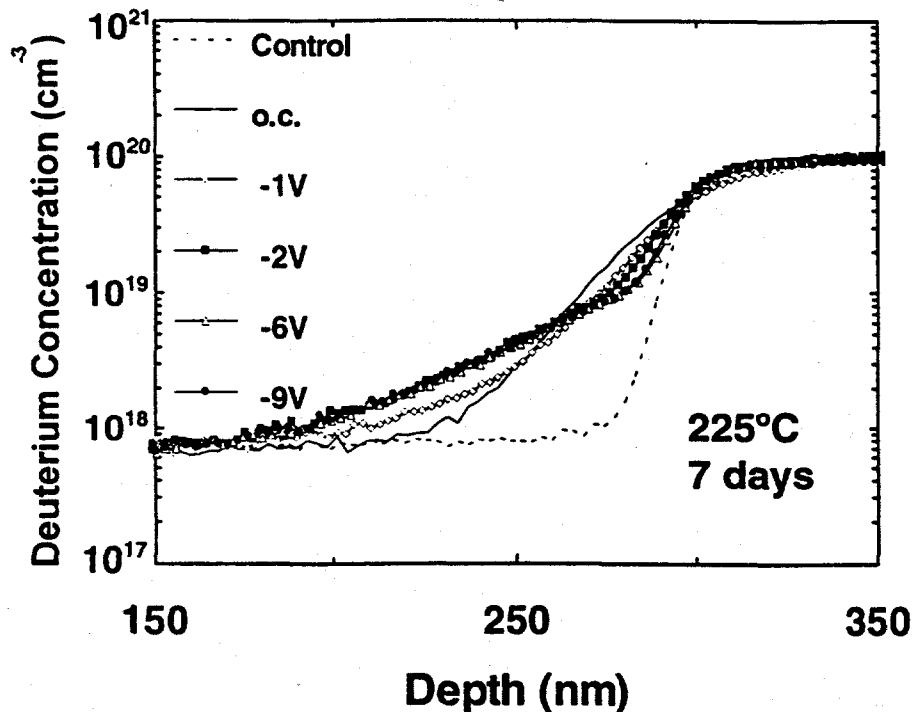

Fig 32. Deuterium concentration profile in the tail region for different applied bias. The dashed and solid lines are the corresponding profiles in an unannealed control, sample and in a sample annealed under open-circuit conditions.

further sharpening of the profiles at the edge of the deuterated layer is observed for reverse biases exceeding 5 V. Results similar to those illustrated in Fig. 32, indicating a strong saturation of the profiles with increasing reverse bias, were obtained in the whole range of temperatures investigated in this study (up to 275°C).

Hydrogen motion in a-Si:H is a trap-limited process where hydrogen must first be excited from a silicon-hydrogen bond into mobile states where it can then diffuse. Both the excitation process and the diffusion through the mobile states are expected to be temperature-dependent processes. Fig. 33 displays diffusion profiles for samples annealed under a fixed reverse bias of 5 V at 225°C (t_d = 7 days), 250°C (t_d = 2 days), and 275°C (t_d = 11 h). For comparison, the solid line reproduces the profile of an as-grown sample. In all cases, the application of a reverse bias leads to a sharpening of the profiles near the edge of the deuterated layer and to the appearance of an exponential tail of fast-migrating atoms. These results indicate that the carrier-assisted (and also temperature-dependent) migration mechanism dominates over a purely thermal hydrogen migration mechanism up to at least 275°C.
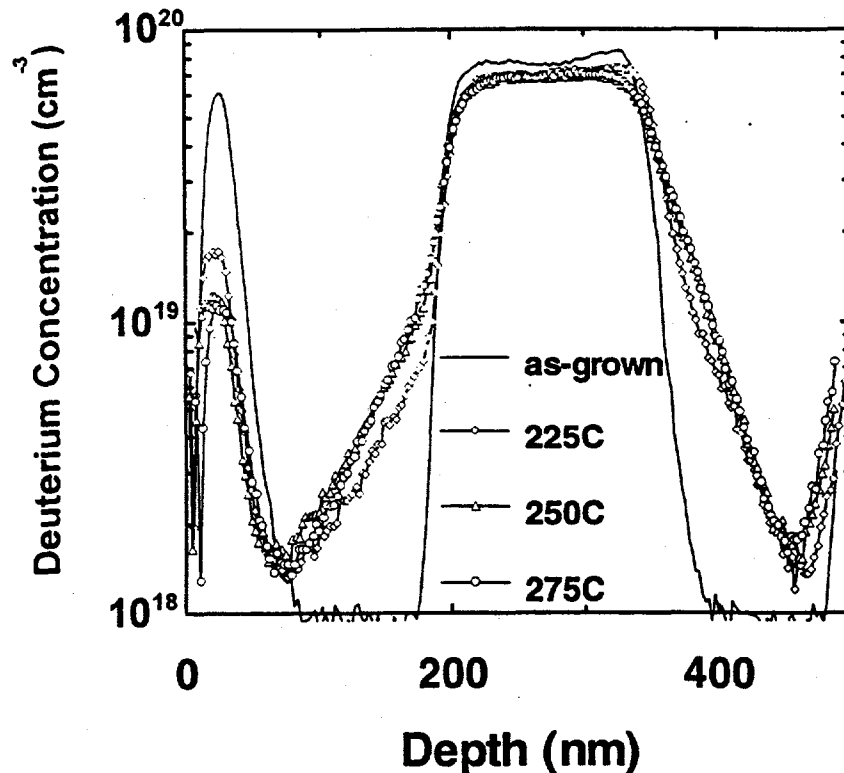

Fig 33. Deuterium concentration profiles in p-i-n diodes annealed under fixed reverse bias of 5V at different temperatures. The solid line is a profile for an as-grown sample. The samples have deuterated n and p contacts.

The samples used in this study have deuterated n- and p-type contact layers. The purpose of the deuteration in this case was to investigate deuterium diffusion in the immediate neighborhood of the p+ and n+ contacts. We noticed, however, that deuterium diffusion from the doped materials into the a-Si:H film is considerably smaller than from an intrinsic a-Si:H:D layer.

The dependence of the deuterium profile on annealing time t_d is illustrated in Figs. 34(a) and (b). The experiments were performed by annealing similar samples for different lengths of time at 225°C [Fig. 34(a)] and at 250°C [Fig. 34(b)]. A fixed reverse bias of 5 V was used in all experiments. The exponential tails appear for short diffusion times as illustrated at 225°C in Fig. 34(a), and their slope does not change significantly with annealing time. Diffusion measurements for longer diffusion times at higher temperatures also show a well-defined exponential tail and a continuous increase in the concentration in the tails with diffusion time. For the longest diffusion times investigated at least half of the hydrogen atoms migrate under reverse bias. This result gives no evidence that the tails are formed by migration of a subset of the deuterium atoms in the a-Si:H:D layer, but rather indicates that the fast migration mechanism leading to the tail formation is accessible to all deuterium atoms.

Fig. 34(c) shows the time dependence of the areal density A_t of deuterium atoms in the exponential tales, obtained by integrating the profiles at the left-hand side of the a-Si:H:D layer after subtraction of the background deuterium concentration present in unannealed samples. The time dependence of A_t can be expressed as $A_t \sim t^a$, with $0.5 < a < 1$. For small A_t, corresponding to short diffusion times and low diffusion temperatures, $a \to 1$ and the deuterium concentration in the tails increases approximately linearly with diffusion time. For large A_t, corresponding to long diffusion times and high diffusion temperatures [see the data for 250°C in Fig. 34(c)]. $a \to 0.5$. This time dependence together with the exponential shape of the profiles indicates that the tails are not formed by a simple diffusion mechanism, for which complementary error function profiles and concentrations proportional to the square root of the annealing time are normally expected.

We conclude that hydrogen migration is controlled by a carrier related mechanisms. Migration is enhanced when the carrier density is increased by
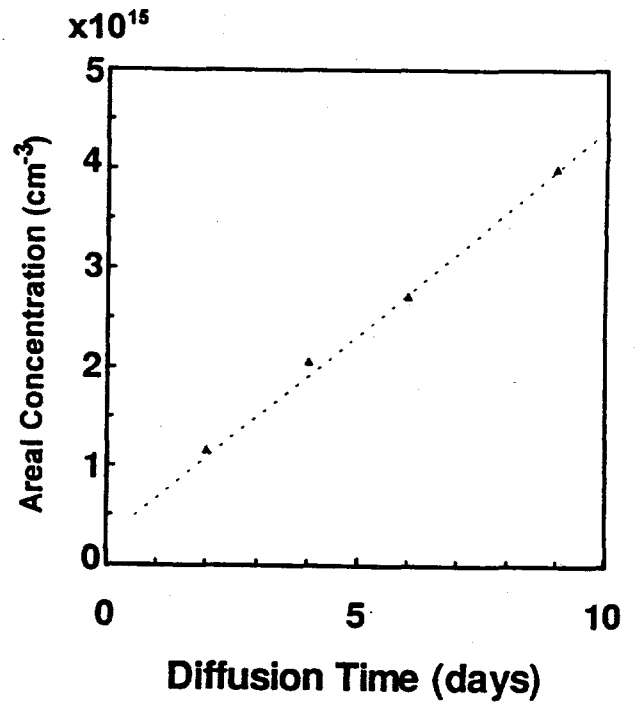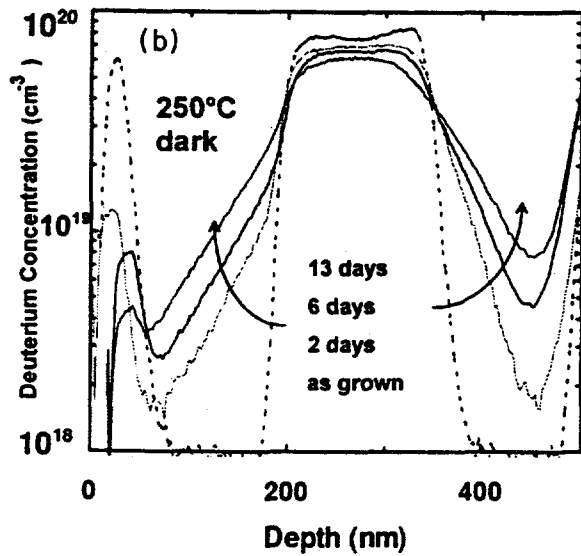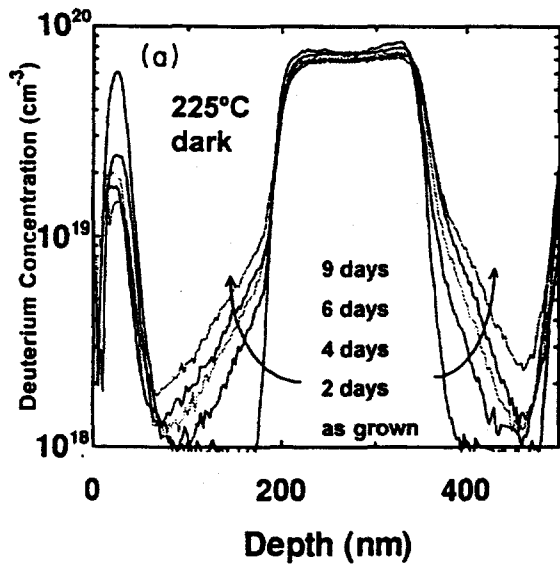
Fig 34. Time dependence of the deuterium profiles after annealing at a fixed reverse bias of 5V and different temperatures (a) and (b). The areal density under the exponential tail is shown in (c)

illumination and is suppressed when carriers are removed from the diffusion region by a reverse bias.

BIBLIOGRAPHY

Nebel, C. E. and Street, R. A. Hall experiments and interpretation on a-Si:H and a-SiC:H (to be published).

Nebel, C. E. and Street, R. A. High field transport in a-Si:H. International Journal of Modern Physics B 7 (1993) 1207.

Nebel, C. E. and Street, R. A. Revealing mysteries of Hall experiments on a-Si:H and a-SiC:H (to be published).

Nebel, C. E., Street, R. A., Jackson, W. B. and Johnson, N. M. Kinetics of metastability in doped A-Si:H (to be published).

Nebel, C. E., Street, R. A. and Johnson, N. M. High-electric-field transport in a-Si:H. I. Transient photoconductivity. Physical Review B 46 (1992) 6789.

Nebel, C. E., Street, R. A., Johnson, N. M. and Tsai, C. C. High-electric-field transport in a-Si:H. II. Dark conductivity. Physical Review B46 (1993) 6803.

Nebel, C. E., Street, R. A., Johnson, N. M. and Walker, J. Electron transport and conduction-band-tail states in a-Si:H deposited with a remote hydrogen plasma (to be published).

Nickel, N. H., Johnson, N. M. and Jackson, W. B. Hydrogen passivation of grain-boundary defects in polycrystalline silicon thin films. Applied Physics Letters 62 (1993) 3285.

Paul, W., Street, R. A. and Wagner, S. Hydrogenated amorphous semiconductors. Journal of Electronic Materials 22 (1993) 39.

Santos, P. V. and Johnson, N. M. Carrier-dependent hydrogen migration in hydrogenated amorphous silicon. Applied Physics Letters 62 (1993) 720.

Santos, P. V., Johnson, N. M., Street, R. A., Hack, M., Thompson, R. and Tsai, C. C. Hydrogen migration and electronic carriers in a-Si:H. Physical Review B47 (1993) 10244.

Schumm, G., Jackson, W. B. and Street, R. A. Non-equilibrium occupancy of tail states and defects in a-Si:H. Implications on defect structure. Physical Review B (to be published)

Schumm, G. Chemical equilibrium description of stable and metastable defect structures in a-Si:H. Physical Review B (to be published)

Street, R. A. Physics of a-Si:H p-i-n devices (to be published).

Street, R. A. Semiconductor of distinction. Physics World (to be published).

Street, R. A., Jackson, W. B. and Hack, M. Comparison of current and light-induced defects in A-Si:H (to be published).

Document Control Page	1. NREL Report No. NREL/TP-451-6192	2. NTIS Accession No. DE94000292	3. Recipient's Accession No.

4. Title and Subtitle	5. Publication Date
Research on the Stability, Electronic Properties, and Structure of a-Si:H and Its Alloys	February 1994
	6.

7. Author(s)	8. Performing Organization Rept. No.
W.B. Jackson, N. Johnson, N. Nickel, C. Nebel, M. Hack, P. Santos, G. Schumm, R.A. Street, R. Thompson, C.C. Tsai, J. Walker	

9. Performing Organization Name and Address	10. Project/Task/Work Unit No.
Xerox Palo Alto Research Center Palo Alto, California 94304	PV431101
	11. Contract (C) or Grant (G) No. (C) HG-1-10063-9 (G)

12. Sponsoring Organization Name and Address	13. Type of Report & Period Covered
National Renewable Energy Laboratory 1617 Cole Blvd. Golden, CO 80401-3393	Technical Report 1 June 1992 - 31 May 1993
	14.

15. Supplementary Notes
NREL technical monitor: B. von Roedern

16. Abstract (Limit: 200 words)

This report describes work focusing on the defect and transport properties of a-Si:H with particular emphasis on defect metastability. Light-induced defects remain the major impediment to higher stabilized solar cell efficiencies. The many years of research have shown that this is a difficult problem to solve, and we take the view that a solution can be found only with a deep understanding of the mechanism; this has been our main goal. The metastability is closely related to the intrinsic defect properties, so these studies have also led to a greatly improved model of all the electronic properties of a-Si:H. Section A of the report discusses a theoretical analysis of the defect pool model for the equilibrium dark defect density, with particular reference to whether there are significant charged defects. Section B discusses the use of an electronic transport model to analyze forward and reverse currents and extends it to the calculation of field dependences of bulk and contact currents, which give more precision to the analysis of defects from reverse bias thermal generation currents. Electronic transport is discussed in Section C. Work done on H transport and bonding is described in Section D.

17. Document Analysis
a. Descriptors
stability ; electronic properties ; structure ; amorphous silicon ; alloys ; photovoltaics ; solar cells

b. Identifiers/Open-Ended Terms

c. UC Categories
271

18. Availability Statement	19. No. of Pages
National Technical Information Service U.S. Department of Commerce 5285 Port Royal Road Springfield, VA 22161	63
	20. Price A04